

THE EFFECTS OF DUST IN SIMPLE ENVIRONMENTS: LARGE MAGELLANIC CLOUD H II REGIONS

ERIC F. BELL, KARL D. GORDON, ROBERT C. KENNICUTT, JR., & DENNIS ZARITSKY

Steward Observatory, University of Arizona, Tucson, AZ 85721

TO APPEAR IN APJ: *January 20 2002, vol. 565, no. 1*

ABSTRACT

We investigate the effects of dust on Large Magellanic Cloud (LMC) H II region spectral energy distributions using arcminute-resolution far-ultraviolet (FUV), H α , far-infrared (FIR), and radio images. Widely-used indicators of the amount of light lost to dust (attenuation) at H α and in the FUV correlate with each other, although often with substantial scatter. There are two interesting systematic discrepancies. First, H α attenuations estimated from the Balmer decrement are lower than those estimated from the H α -to-thermal radio luminosity ratio. Our data, at this stage, cannot unambiguously identify the source of this discrepancy. Second, the attenuation at 1500Å and UV spectral slope, β , correlate, although the slope and scatter are substantially different from the correlation first derived for starbursting galaxies by Calzetti et al. Combining our result with those of Meurer et al. for ultra-luminous infrared galaxies and Calzetti et al. for starbursting galaxies, we conclude that no single relation between β and 1500Å attenuation is applicable to all star-forming systems.

Subject headings: dust, extinction — H II regions — Magellanic Clouds — galaxies: individual (LMC) — ultraviolet: galaxies

1. INTRODUCTION

Estimating where and how quickly stars are forming in galaxies of different types, as a function of redshift, gives us direct insight into where, when and how galaxies evolve (see e.g. Madau et al. 1996; Blain et al. 1999; Steidel et al. 1999, for attempts to address this problem in a global sense). In this context, understanding the systematic uncertainties plaguing SFR estimators is of special importance. One of the principal uncertainties of this type is the correction for emergent flux lost due to dust. In a systematic effort to address this problem, we begin by studying the effects of dust in the simplest of all star formation environments, H II regions.

Before discussing the effects of dust, it is necessary to understand the nature and origins of the different SFR indicators. SFRs are usually estimated from spectral regions where the energy output from young stars dominates. Massive, short-lived stars produce copious quantities of ultraviolet (UV) radiation. This UV light may be directly observed, or dust may absorb much of it, reprocessing it into the far-infrared (FIR). In the limit of dust absorbing all of the energy output of young stellar populations, the FIR radiation is approximated by the bolometric luminosity. The time evolution of the UV and bolometric luminosities is shown in Fig. 1 for a single burst from the PÉGASE stellar population models (Fioc & Rocca-Volmerange 2001): the UV and bolometric luminosities evolve similarly for more than 100 Myr. The most massive and short-lived stars produce radiation capable of ionizing the hydrogen gas in their natal clouds, producing a H II region. This ionized hydrogen plasma produces line emission (the Balmer series is the most frequently observed series of emission lines) and thermal bremsstrahlung in the radio: these radiations evolve much more quickly than the 1500Å UV or bolometric luminosities (Fig. 1).

However, the H α and UV luminosities will be strongly reduced by dust. The amount of light lost from a system is referred to as the *attenuation*. The attenuation and the more commonly used *extinction* are the same for a single star with dust along the line-of-sight. However, for more complex systems, the attenuation is a function of the geometry of both the dust and stars. Classic methods that work for determining extinc-

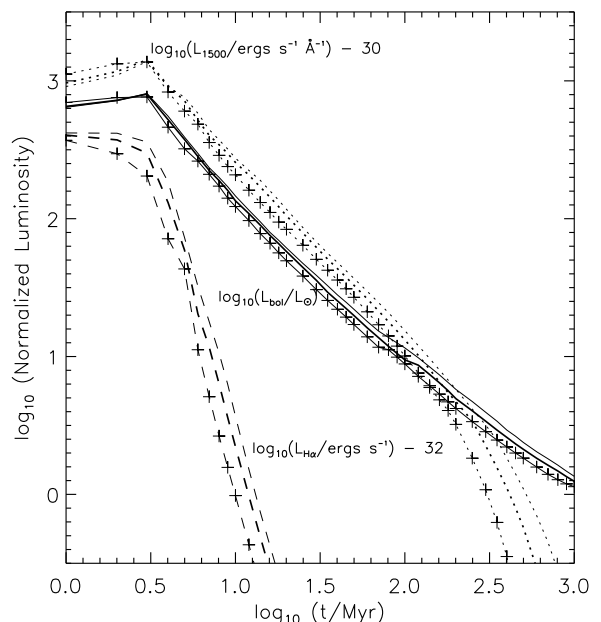


FIG. 1.— Age and metallicity dependence of the bolometric luminosity (L_{bol} ; solid lines), 1500Å luminosity (L_{1500} ; dotted lines), and H α luminosity ($L_{\text{H}\alpha}$; derived assuming 0.45 H α photons per Lyman continuum photon; dashed lines) of a $1M_{\odot}$ stellar population, as derived using the PÉGASE stellar population synthesis models (Fioc & Rocca-Volmerange 2001). Thick lines denote the $Z=0.008$ (40% solar) models, thin lines denote the $Z=0.004$ (20% solar) models, and thin lines with crosses denote the $Z=0.02$ (solar) models. All luminosities at ages $\gtrsim 3$ Myr decrease with increasing metallicity, primarily due to increased stellar opacities. At younger ages, the behavior is more complex because of the interplay of mean molecular weight and opacity effects.

tions (e.g. color excesses) will not reliably determine attenuations.

Despite the difficulties introduced by geometry, it is possible to estimate the amount of luminosity lost at H α or in the UV, allowing the true SFR to be estimated. Some attenuation estimators rely solely on UV/optical data. For example, it is common

to estimate the amount of $H\alpha$ light lost to dust by comparing the $H\alpha$ and $H\beta$ emission-line fluxes, which have an intrinsic ratio fixed by atomic physics in most astrophysical environments. The observed relative ratio therefore gives an estimate of the reddening: this can be transformed into an attenuation under the assumption of a particular attenuation curve (see e.g. Quillen & Yukita 2001, for a test of this method, and references therein). A common approach to estimate the attenuation of UV stellar light is to use the UV spectral slope β . This approach, pioneered by Calzetti et al. (1994) and Meurer, Heckman, & Calzetti (1999), uses the relatively narrow range in intrinsic β for young, luminous stellar populations ($-2.6 < \beta < -1.5$ including even metal-rich single bursts with ages younger than 20 Myr; Leitherer et al. 1999) to estimate the reddening. This reddening is observed to correlate with UV attenuation with only modest scatter for local starbursting galaxies (Calzetti et al. 1994; Heckman et al. 1998; Meurer, Heckman, & Calzetti 1999). However, if one applies this relationship to systems other than those for which it was calibrated, then one is assuming that the relation holds over a variety of star-forming systems.

Other attenuation estimators rely on data from beyond UV and optical wavelengths. For example, the $H\alpha$ attenuation can be estimated from the ratio of $H\alpha$ to thermal radio continuum (e.g. Israel & Kennicutt 1980; Kennicutt 1983; van der Hulst et al. 1988). In this case, one concern is that the thermal radio emission may be contaminated by non-thermal emission. This contamination is severe for most galaxies (in fact, the non-thermal radio may correlate with SFR, although we do not discuss it in this paper; see e.g. Condon 1992; Cram et al. 1998). Another such attenuation indicator, this time for the far-UV (FUV), uses the ratio of FUV to FIR, which measures the amount of FUV light reprocessed into the FIR (e.g. Buat & Xu 1996; Meurer, Heckman, & Calzetti 1999; Gordon et al. 2000).

There are inevitable limitations to any attenuation estimator. Bearing in mind the importance of constructing relatively accurate, unbiased SFRs as a probe of galactic evolution, it is vital to critically assess the applicability and efficacy of attenuation estimators. Considering data from as many wavelengths as possible is an important part of this assessment: by using UV, $H\alpha$, FIR, and thermal radio luminosities it is possible to construct different estimates of the attenuation at a given wavelength. Examples of this kind of multi-wavelength approach for galaxies include Calzetti et al. (1994), Meurer, Heckman, & Calzetti (1999), Sullivan et al. (2000), and Bell & Kennicutt (2001).

An essential test of the robustness of attenuation indicators is their behavior in the simplest of all composite star-forming systems: H II regions. Without a firm understanding of the attenuation of $H\alpha$ and FUV light in H II regions, we cannot claim a firm understanding of the effects of dust on galactic scales. Because H II regions have ionized gas and relatively well-constrained ages (the dominant populations have to be capable of ionizing hydrogen), it is possible to intercompare the attenuations derived for the ionized gas and those derived for the stellar population inside the H II region. We have chosen to use the sample of Large Magellanic Cloud (LMC) H II regions from Caplan & Deharveng (1986) for this purpose. This sample of H II regions has a number of advantages for this purpose: a common distance, modest galactic foreground extinction, and the availability of large-format images and published data in the UV, optical, FIR, and radio spectral regions with a useful physi-

cal resolution (we adopt $4.9'$ [80 pc] diameter apertures for this work).

The remainder of this paper is organized as follows. §2 discusses the construction and limitations of FUV and $H\alpha$ attenuation indicators. §3 describes the multi-wavelength imaging data, the morphology of the LMC at different wavelengths, and the photometry of individual H II regions. §4 quantifies the relationships between different H II region attenuation indicators. In §5, we discuss in detail two particular comparisons: the well-documented discrepancy between $H\alpha$ attenuations estimated from Balmer decrements and $H\alpha$ -to-radio ratios, and the highly scattered and rather steep correlation between FUV attenuation and UV spectral slope β . §6 summarizes our conclusions from this study. We assume a distance to the LMC of 45.9 ± 2 kpc (e.g. Fitzpatrick et al. 2001), which only affects the absolute scaling of the SEDs presented in §3 because the attenuations and flux ratios are distance-independent. In correcting our attenuation estimates for foreground galactic extinction, we adopt a foreground reddening of $E(B-V) = 0.06$, following Schlegel et al. (1998) and Oestreicher, Gochermann, & Schmidt-Kaler (1995).

2. QUANTITATIVE ATTENUATION INDICATORS

In this section, we discuss the estimation of $H\alpha$ and UV attenuations from multiwavelength data. This serves a dual purpose: to introduce the methods used to calculate the attenuation indicators later in the paper, and to instill an intuition for what to expect when comparing the different attenuation indicators, including the nontrivial effects of radiative transfer.

2.1. Attenuation of far-UV light

Using measured UV reddenings to estimate the FUV attenuation is becoming increasingly fashionable due to its observational efficiency. The UV continuum spectral slope β , defined by:

$$F_{\lambda} \propto \lambda^{\beta}, \quad (1)$$

where F_{λ} is the flux per unit wavelength λ , is used to estimate the attenuation in the UV (e.g. Calzetti et al. 1994; Meurer, Heckman, & Calzetti 1999; Adelberger & Steidel 2000) because one presumes to understand the color of the underlying starlight, and so any deviation from this color is attributed to dust. To the degree that one believes the underlying assumptions in this method, one could, for example, also use optical reddenings to estimate UV attenuation, or use UV reddenings to estimate the optical attenuation. Clearly, such an exaggerated extension of the technique loses credibility and one begins to wonder where, exactly, the technique may break down. The relationship between the UV or optical reddenings and the FUV attenuation is non-trivial, as illustrated in panels (a) and (b) of Fig. 2.

In Fig. 2, we show predictions from the radiative transfer model DIRTY (Witt & Gordon 2000; Gordon et al. 2001; Misselt et al. 2001). The relationships between different attenuation indicators are shown under different assumptions about the extinction curve (MW=Milky Way, LMC2=a supershell near 30 Dor, SMC=Small Magellanic Cloud Bar), dust clumping (homogeneous or clumpy, with a density ratio of 100), and geometry (dusty=uniformly mixed stars and dust, shell=inner dust-free region of stars surrounded by a shell of star-free dust). The main point to note from the panels (a) and (b) of Fig. 2 is that it is possible to have a large range in FUV attenuation for a given

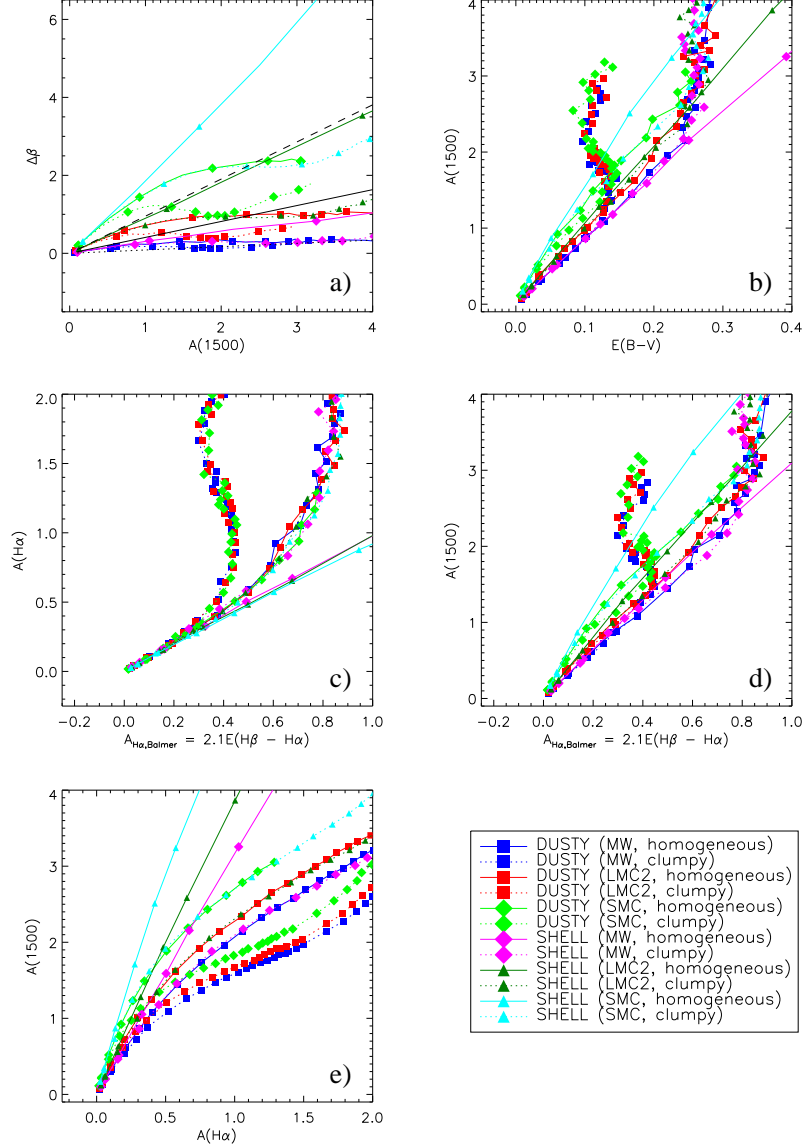


FIG. 2.— Predictions from radiative transfer models regarding the relationships between different attenuation indicators. (a) 1500Å attenuation against change in UV spectral slope $\Delta\beta$, (b) $E(B-V)$ against 1500Å attenuation, (c) Balmer-derived $H\alpha$ attenuation against true $H\alpha$ attenuation, (d) Balmer-derived $H\alpha$ attenuation against 1500Å attenuation, and (e) true $H\alpha$ attenuation against 1500Å attenuation. Models are described in the legend, and expanded on in the text. Panel (a) also shows screen models with LMC (solid line) and SMC Bar (dashed line) extinction curves.

UV or optical reddening, depending on the dust/star geometry and/or shape of extinction curve. Bearing in mind the extensive empirical evidence for a highly environmentally-sensitive UV extinction curve (e.g. Fitzpatrick 1986; Gordon & Clayton 1998; Misselt, Clayton & Gordon 1999; Clayton, Gordon, & Wolff 2000), and the diversity of dust/star geometries observed in many astrophysical systems, our expectation is that the validity of UV or optical reddening-based attenuations is open to suspicion in any but the best-studied and characterized cases.

It is possible to avoid the need to assume a particular extinction curve in deriving the FUV attenuation by comparing the observed FUV starlight with the FIR luminosity. Because the majority of the bolometric flux of a young stellar population is emitted in the FUV and because the FIR flux is dominated by the re-radiation of attenuated UV light, this comparison provides an estimate of the FUV attenuation that is insensitive to the extinction curve and geometry when averaged over 4π steradians

(see Figs. 1 and 2 of Gordon et al. 2000). We use an IDL subroutine, available from K. D. G., and described fully in Gordon et al. (2000), to estimate the attenuation at 1500Å and 1900Å from the 1500Å, 1900Å, and FIR fluxes. This subroutine takes into account the full uncertainties implied by differences in dust geometry, dust type and stellar populations. For 1500Å attenuations between 0 and 4 mags, the 1500Å flux ratio method-derived attenuation can be approximated by a modification of the simple energy-balance estimate to within 0.03 mag:

$$A_{1500,FR} \sim 0.86 \left[-2.5 \log_{10} \frac{\nu f_{\nu}}{\nu f_{\nu} + L_{FIR}} \right] - 0.1, \quad (2)$$

where the bracketed quantity is the simple energy-balance estimate of 1500Å attenuation (νf_{ν} is evaluated at 1500Å), L_{FIR} is an estimate of the total FIR luminosity (estimated as described in §4.2.1), and the scaling and subtraction approximately correct for SED and attenuation curve shape. This method has

important limitations. First, it requires isotropy on scales larger than the illuminating source. An example of a geometry for which this approach fails is the case of a torus of dust outside a cluster of FUV-bright stars, in which the torus is oriented perpendicular to the line of sight. Such a region would have a large FIR luminosity but *no* attenuation along the line of sight. Second, the method requires the young population to dominate the heating. The method, some of its uncertainties, and its limitations are presented in Gordon et al. (2000): variants of this method were used by e.g. Buat & Xu (1996) or Meurer, Heckman, & Calzetti (1999) to explore the attenuations of spiral and starburst galaxies respectively.

2.2. Attenuation of H α light

Estimating the H α luminosity lost to dust is relatively straightforward. We discuss two methods: both estimate only the attenuation of the H α radiation and are insensitive to the amount of Lyman continuum radiation lost to dust before being down-converted into H α . The first is based on the comparison of the H α line luminosity to the thermal radio luminosity. This ratio, in the absence of dust, is given by equations A5 and A10 of Caplan & Deharveng (1986):

$$f_{\text{H}\alpha}/f_{8.55\text{GHz}} = 8.659 \times 10^{-9} \text{ erg cm}^{-2} \text{ s}^{-1} \text{ Jy}^{-1} \times (t_e)^{-0.44} [8.666 + 1.5 \ln(t_e)]^{-1}, \quad (3)$$

where $f_{\text{H}\alpha}$ is the H α flux in $\text{erg cm}^{-2} \text{ s}^{-1}$, $f_{8.55\text{GHz}}$ is the 8.55 GHz flux in Jy, and t_e is the electron temperature in units of 10^4 K . The ratio depends weakly on electron temperature: we will adopt an electron temperature of $9500 \text{ K} \pm 1000 \text{ K}$ (Pagel et al. 1978), corresponding in dust-free H α to radio ratio uncertainties of $\sim 8\%$. In practice, the thermal radio luminosity is used to construct an expectation for the H α line luminosity. Then, the observed H α line luminosity is compared to the radio expectation to derive an effective attenuation $A_{\text{H}\alpha, \text{Radio}}$. Although this should be a robust attenuation indicator, accurate *thermal* radio luminosities are difficult to measure, even for individual H II regions.

The second approach is to estimate the H α attenuation using the observed H α /H β ratio for a given H II region. Assuming a standard $R_V = 3.1$ Milky Way extinction curve and a foreground screen dust distribution, Caplan & Deharveng (1986) derive the following expression for H α attenuation estimated from the Balmer decrement $A_{\text{H}\alpha, \text{Balmer}}$ given an observed H α /H β :

$$A_{\text{H}\alpha, \text{Balmer}} = 5.25 \log_{10} \left(\frac{\text{H}\alpha/\text{H}\beta}{2.859 t_e^{-0.07}} \right), \quad (4)$$

or, equivalently, $A_{\text{H}\alpha, \text{Balmer}} = 2.1 E(\text{H}\beta - \text{H}\alpha)$. H α /H β is observationally straightforward to measure; however, different dust extinction curves or geometries change the conversion between reddening and attenuation from the standard $R_V = 3.1$ foreground screen.

The sensitivity of these estimators to geometry and dust properties is illustrated in panel (c) of Fig. 2, where $A_{\text{H}\alpha, \text{Balmer}}$ is shown against the true H α attenuation $A(\text{H}\alpha)$. For homogeneous shell or screen geometries, $A_{\text{H}\alpha, \text{Balmer}}$ and $A(\text{H}\alpha)$ are essentially identical; however, clumpy shell and dusty geometries show a ‘saturation’ for $A_{\text{H}\alpha, \text{Balmer}} \sim 0.8$ and $\sim 0.4 \text{ mag}$ respectively, where only the least reddened stars are observed, resulting in high attenuations but modest reddenings.

2.3. Comparing H α and far-UV attenuations

The relationship between H α and FUV attenuations is complex because it depends on extinction curve shape, dust clumping properties, and geometry (panel (d) of Fig. 2). In particular, for clumped dust or mixed star/dust geometries, the relationship between $A_{\text{H}\alpha, \text{Balmer}}$ and 1500Å attenuation is non-linear. Panel (d) is quite similar to panel (b); both $A_{\text{H}\alpha, \text{Balmer}}$ and $E(B-V)$ are essentially color excesses, and behave quite similarly. Also, as shown in panel (e), the relationship between true H α and 1500Å attenuation is non-linear for clumped and/or dusty geometries (in quite a different way than the Balmer-derived H α attenuation). While the FUV attenuation ‘saturates’ at around 2 magnitudes, the H α attenuation continues to increase (because the FUV becomes optically thick, but the H α remains optically thin). A further complication, which is more of a concern when comparing H α and FUV attenuation in galaxies, is that the H α and FUV light can come from spatially distinct locations. In H II regions, this is less of a concern, and we will use the inter-comparison of H α and FUV attenuations to test the reproducibility of these attenuation estimators.

3. DATA ANALYSIS

3.1. Images

We use FUV, H α , FIR, and 8.55 GHz radio images of the LMC to investigate the spectral energy distributions (SEDs) and attenuations for H II regions drawn from the catalogs of Caplan & Deharveng (1985, 1986). Accordingly, we have compiled an extensive library of LMC images with roughly arcminute resolution from the literature. We describe these images in turn below, and in Table 1.

- The UV images come from a rocket launched from Australia in 1977 (for a full description see Smith, Cornett, & Hill (1987)). The angular resolution is $\sim 100''$ over most of the useful part of the image. We convert the raw digital units to MJy/sr using calibrations supplied by R. Cornett (1999, private communication). We rule out offsets in calibration larger than 12% at the 2σ level by comparing to aperture fluxes of 10 star form-

TABLE 1
LMC DATA

Band	λ [μm]	$\Delta\lambda$ [μm]	FWHM [$''$]	Ref
Rocket_UV1	0.1495	0.020	100	1
Rocket_UV2	0.1934	0.022	100	1
R	0.66	0.15	72	2
H α	0.6571	0.0013	72	2
MSX B3	8.3	3.36	45	3
IRAS 12 μm	12	6.5	38	4
IRAS 25 μm	25	11	42	4
IRAS 60 μm	60	40	75	4
IRAS 100 μm	100	37	135	4
8550 MHz	3.5×10^4	...	210	5

References. — (1) Smith, Cornett, & Hill (1987), (2) Kennicutt et al. (1995), (3) <http://www.ipac.caltech.edu/ipac/msx/msx.html>, (4) Braun et al. (1998), (5) Filipović et al. (1998)

ing regions from *Ultraviolet Imaging Telescope* images with an effective wavelength of 1614Å.

- The $H\alpha$ and R band images were taken with the Parking Lot Camera (Bothun & Thompson 1986), but with a Texas Instruments 800×800 pixel CCD (Kennicutt et al. 1995). We calibrated the $H\alpha$ image by comparing to aperture $H\alpha$ fluxes from Caplan & Deharveng (1985). Our calibration is consistent with the calibration of the $H\alpha$ image given by Kennicutt et al. (1995) to within 10%. The R band image has not been photometrically calibrated.
- The *Midcourse Space Experiment* (MSX) B3 (8.3 μ m) data were downloaded from the IPAC MSX site (for a description of the instrument and the data see Price et al. 2001). We use the mosaic image, with 45'' instead of 18'' resolution, as our work is limited by the lower resolutions of the images in other passbands.
- The IRAS images at 12 μ m, 25 μ m, 60 μ m and 100 μ m, processed with a maximum entropy algorithm to improve resolution (Braun et al. 1998), were provided by M. Braun (2000, private communication). We confirm the validity of structures seen in the resolution-enhanced images by comparing the processed IRAS 12 μ m image with the MSX 8.3 μ m image. The morphologies of the structures in the images are very similar. At faint levels, the processed image displays the characteristic striping of IRAS data.
- The radio images were provided by M. Filipović (2000, private communication) and are described in detail in Filipović et al. (1998). These data are calibrated to better than 15%, when tested against ‘aperture’ 5 GHz radio fluxes from Caplan & Deharveng (1986): before comparison, the 5 GHz radio fluxes were scaled down by 5% to account for wavelength differences, assuming purely thermal radio emission.

All the images were aligned (translation and rotation only) to the R band image, for which J. Parker (1999, private communication) provided an astrometric solution. At least 5–10 stars and H II regions were used as the basis of the alignment, and alignment was accurate to better than 20'' in all cases. After the alignment, the images were transformed to a common NCP projection with 30'' pixels. All of the images, except for the $H\alpha$ and R band image, are calibrated in units of MJy/sr. The $H\alpha$ image is calibrated in $\text{ergs s}^{-1} \text{cm}^{-2}$ and, as stated before, the R band image is uncalibrated. The original and calibrated, aligned images are available from the authors.

3.2. Morphology of the LMC at different wavelengths

Before discussing the SEDs and attenuations of the LMC H II regions, we must comment on one of the most striking aspects of Fig. 3 — the strong difference between the distributions of the young stars (as probed by the $H\alpha$, 1900Å or FIR emission) and older stars (as probed by the R band). The older stellar populations are strongly concentrated in the bar, with an underlying disk-like envelope. In contrast, the younger stars have a clumpy distribution, and are predominantly concentrated in the northern half of the LMC. This interesting aspect of the data is beyond the scope of the current work.

More subtle, but perhaps equally significant, differences are also present. In §1, we saw that the UV and FIR luminosities should track each other quite closely if the amount and distribution of dust around young stars does not depend on stellar age. Therefore, a naïve expectation might be that the morphologies of the LMC in the UV and FIR should be similar. In contrast, the $H\alpha$ morphology could either be similar or not depending

on the detailed star formation history over timescales of ~ 10 to 100 Myr. Surprisingly, the observation is that the FIR and $H\alpha$ morphologies are similar (cf. Fig. 3), and that they differ from the morphology in the UV.

This departure from the naïve model has two interesting implications. Firstly, the assumption used in linking UV to FIR luminosities has broken down. The similarity between the $H\alpha$ and FIR morphologies implies that there is a good correspondence between the distribution of very young (ionizing) stars and dust. However, as stars age (so that they are now no longer strongly ionizing stars but still have relatively large UV fluxes), the distribution of dust must decouple from that of the stars. We suggest the simple scenario in which young, dusty H II regions are dispersed by the cumulative effects of stellar winds and supernovae. This dispersal (1) causes many of the FUV-bright regions to be faint in the FIR, (2) explains the existence of large, extended FUV-bright regions ringed by $H\alpha$ and FIR emission from recent star formation, that are triggered by the winds from the OB association in the center (e.g. Constellation III, in the top left quadrant of the images), and (3) is consistent with other empirical evidence (e.g. Charlot & Fall 2000, and references therein).

Secondly, the dissimilarity between the $H\alpha$ and UV morphologies of the LMC stresses a fundamental limitation of this work in its application to the global situation in galaxies. Because much of the UV flux of the LMC comes from outside the H II regions we study here, we cannot meaningfully constrain the effects of dust on the total UV emission from the LMC (we will address this issue in future work). The dichotomy between the sites of $H\alpha$ and UV emission also leads us to caution against attempts to link the effects of dust on galactic $H\alpha$ and UV emission too closely: it may be impossible to meaningfully link the $H\alpha$ and FUV extinction properties of star-forming galaxies in any more than a statistical sense.

3.3. SEDs

We selected a sample of H II regions with measured Balmer decrements in 4.9' diameter apertures from the sample of Caplan & Deharveng (1985, 1986). We retained the use of the 4.9' aperture to ensure a common aperture for all attenuations: the adoption of a larger aperture (up to 20', depending on source size and morphology) gave very similar attenuations at better than the 10% level (and similar values of UV spectral slope β at better than the 0.5 level). The locations of the H II regions are indicated in Fig. 3. An explicit selection was made for isolation: any H II regions from Caplan & Deharveng (1985, 1986) with significant contamination at any wavelength (determined visually) from other, nearby H II regions were omitted from the sample.

To correct aperture flux measurements for ‘sky’ contamination, local sky levels are estimated using a centered annulus with an inner radius of 20' and an outer radius of 30'. The sky annulus is split into octants, and the median level within each octant is determined. In constructing the mean and RMS of the local sky, the highest three octants are discarded, to ensure against contamination of the sky level by nearby emission. In (rare) cases where there is no nearby emission, this approach results in a slight systematic underestimate of at most 1σ in the sky level, or a corresponding overestimate of at most a few percent in the H II region flux. In most cases, however, this method largely negates the effects of emission in the sky annulus and reproduces manually estimated sky levels to within 1σ with no

FIG. 3.— The morphology of the LMC at $H\alpha$, 1900Å, R band, and in the FIR 60 μ m band. The 52 H II regions in our sample are circled.

hint of systematic offset.

Aperture corrections are typically not required for most of the data. However, because the FWHM of a point source in the 8.55 GHz radio map is 210'', a modest aperture correction is applied. We derive this aperture correction empirically by smoothing the observed image with a 210'' FWHM Gaussian beam and comparing the aperture flux in the convolved and original images. The ratio of these fluxes is adopted as the aperture correction. This procedure is tested by re-convolving the convolved image (i.e. how well can one recover the flux in the original image by aperture correcting the flux measured from the convolved image). This procedure appears to be accurate to $\sim 5\%$. Typical aperture corrections are $\sim 15\text{--}25\%$, depending on aperture size and source morphology.

Color correction in the FUV and FIR is required (the $H\alpha$ and radio do not require color correction because of the narrow bandpasses). Fluxes are corrected to the nominal effective wavelength of the filters. FUV color corrections, in terms of the observed 1500Å to 1900Å flux ratio, are calculated using a sequence of *IUE* spectra that are artificially reddened using a SMC extinction curve (used because it lacks a 2200Å bump, leading to a more stable color correction). Using different *IUE* spectra and/or a LMC extinction curve to artificially redden the spectra leads to differences in color correction smaller than $\sim 3\%$. FIR color corrections are estimated from the observed 60 μ m to 100 μ m flux ratio, using the multiplicative corrections from the *IRAS* Explanatory Supplement (1.09 ± 0.01 at 60 μ m and 1.01 ± 0.01 at 100 μ m, for the range of observed H II region FIR colors). Color correction for the 8.3 μ m, 12 μ m, and 25 μ m fluxes was not attempted due to the complexity of the FIR spectrum at those wavelengths and negligible contribution of the FIR emission from those wavelengths to the integrated FIR emission.

In Fig. 4, we show examples of our H II region SEDs (omitting the radio flux point because it makes a negligible contribution to the total bolometric flux of a star formation region, and the $H\alpha$ data point because it is line emission). The error bars (which are in some cases smaller than the plotted symbol) reflect sky level uncertainties: a 5% uncertainty is added to the sky error in the FUV to account for the color correction (and adding an arbitrary modest contribution for ‘flat fielding’). A 5% uncertainty is added to the sky error in the radio to account for aperture correction errors. $H\alpha$ errors include an arbitrary 5% flat fielding and continuum subtraction uncertainty. Calibration and image alignment uncertainties are not accounted for in the error bars. We do not correct for foreground galactic extinction in constructing the SEDs, but correct for it when quantifying the H II region attenuations. We present the H II region fluxes and uncertainties within the 4.9' apertures in Table 2. The fluxes in this Table *have not* been corrected for galactic foreground extinction.

4. THE EFFECTS OF DUST IN LMC H II REGION SEDS

Fig. 4 illustrates the significant effect of dust on H II region SEDs. As expected, increasing amounts of dust progressively depress the UV flux, re-processing this energy into the FIR. By using our understanding of the physics of nebular emission and the spectra of different stellar populations, we can produce quantitative attenuation estimates. In this section, we

apply the various attenuation estimators described previously and compare the results. For reference, our measurements of the H II region attenuation and UV spectral slope β within the 4.9' apertures, corrected for foreground galactic extinction, are presented in Table 3.

4.1. Comparing estimates of $H\alpha$ attenuation

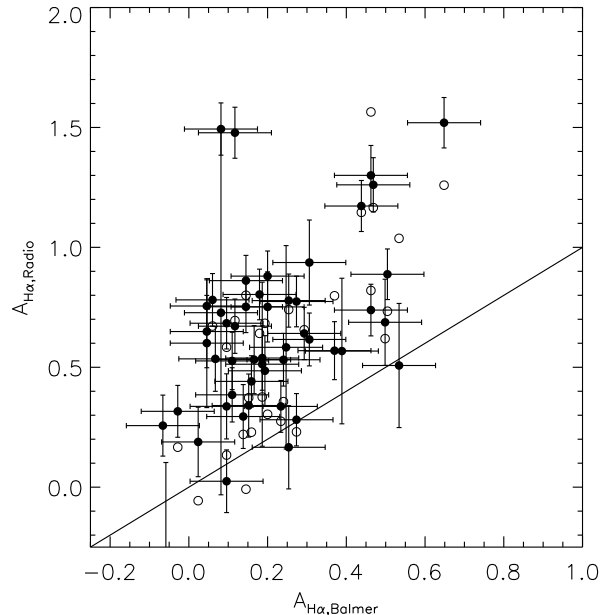


FIG. 5.— Solid points denote radio-derived $H\alpha$ attenuations ($A_{H\alpha, \text{Radio}}$) against Balmer-derived attenuations ($A_{H\alpha, \text{Balmer}}$), using the 4.9' aperture of Caplan & Deharveng (1985, 1986) for 50 of our 52 H II regions. The Balmer-derived attenuation $A_{H\alpha, \text{Balmer}}$ is derived using $H\alpha/H\beta$ values from Caplan & Deharveng (1985). Open points denote the radio-derived attenuations from Caplan & Deharveng (1986), for the 29 H II regions in common with our clipped sample of 50 H II regions. The solid line denotes the relationship expected if $A_{H\alpha, \text{Balmer}}$ equals $A_{H\alpha, \text{Radio}}$.

Caplan & Deharveng (1986) found that radio-derived $H\alpha$ attenuations of LMC H II regions, $A_{H\alpha, \text{Radio}}$, exceeded the Balmer-derived $H\alpha$ attenuations, $A_{H\alpha, \text{Balmer}}$. This result was confirmed using independent radio data for LMC H II regions (Ye 1998) and for H II regions in M51 (van der Hulst et al. 1988). This systematic offset was attributed to clumped dust, which makes the effective attenuation curve grayer (cf. panel (c) of Fig. 2).

We re-examine this question using $H\alpha/H\beta$ values from Caplan & Deharveng (1985) corrected for Galactic extinction, in conjunction with $A_{H\alpha, \text{Radio}}$ values derived from our galactic extinction-corrected aperture $H\alpha$ fluxes and aperture-corrected radio fluxes. We discard N30BC (no Balmer decrement) and N158A (radio detection less than 2σ). Uncertainties in $A_{H\alpha, \text{Radio}}$ come from propagating the uncertainties in the SED measurements and the adopted electron temperature. The uncertainty in $A_{H\alpha, \text{Balmer}}$ is calculated to be 9% by propagating a 4% uncertainty in $H\alpha/H\beta$ (Caplan & Deharveng 1985) and the uncertainty in the electron temperature. We plot our values for $A_{H\alpha, \text{Radio}}$ and $A_{H\alpha, \text{Balmer}}$, the line of equality for reference, and the original data from Caplan & Deharveng (1986) in Fig. 5.

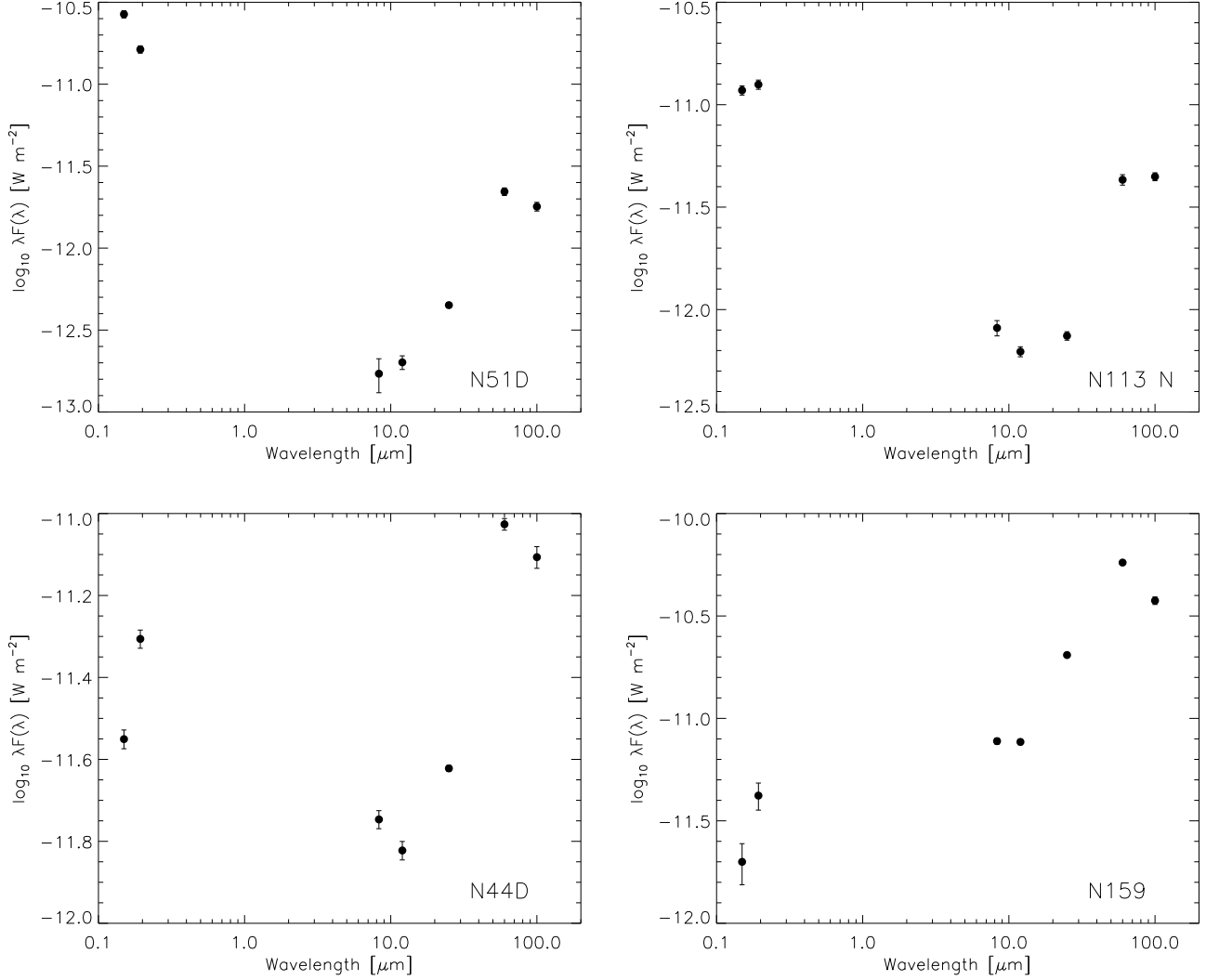


FIG. 4.— SEDs in $4.9'$ apertures for four H II regions, sorted by extinction (left to right; top to bottom): N51D (~ 0 mag at $H\alpha$), N113 N (~ 0.15 mag at $H\alpha$), N44D (~ 0.25 mag at $H\alpha$), and N159 (~ 0.6 mag at $H\alpha$). The $H\alpha$ extinctions are determined using the Balmer decrement within $4.9'$ as measured by Caplan & Deharveng (1985), assuming a Milky Way extinction curve and a foreground screen dust distribution. The logarithm of the energy flux λF_λ in W m^{-2} is shown at 1500\AA , 1900\AA , $8.3\mu\text{m}$, $12\mu\text{m}$, $25\mu\text{m}$, $60\mu\text{m}$, and $100\mu\text{m}$. The $8.3\mu\text{m}$ flux can be larger than the $12\mu\text{m}$ flux due to emission from the unidentified infrared bands, most plausibly associated with polycyclic aromatic hydrocarbons (e.g. Puget & Léger 1989). These data are not corrected for foreground galactic extinction, but are color-corrected (see text for details). Note that some error bars are smaller than the plotting symbols.

For 29 H II regions in common we find a good overall agreement between our values of $A_{H\alpha, \text{Radio}}$ and those from Caplan & Deharveng (1986), with a mean offset of 0.1 mag (ours are larger) and RMS of 0.3 mag. Omitting the 4 H II regions with discrepancies larger than 0.5 mag (three high values and one low value) reduces the offset to 0.06 mag and the RMS to 0.14 mag. For reference, our median $A_{H\alpha, \text{Radio}}$ formal uncertainty for these 29 H II regions is 0.11 mag. We confirm the offset between $A_{H\alpha, \text{Radio}}$ and $A_{H\alpha, \text{Balmer}}$ observed by Caplan & Deharveng (1986): we discuss the origin of this offset in §5.1.

4.2. Comparing estimates of far-UV attenuation

We now assess the consistency of indicators of the attenuation suffered by the starlight from young stellar populations. We compare reddening estimates, and inter-compare these with estimates of the attenuation in the UV derived using UV/FIR energy balance. When comparing these attenuation indicators, we also present the naïve expectation from a screen model with

LMC and SMC Bar-type dust. The intention of showing these models is to enable one to use existing intuition to help understand the results. These models do not represent the true situation. In particular, it would be incorrect to differentiate between possible extinction curves on the basis of these data because radiative transfer effects complicate the interpretation of these plots.

4.2.1. Estimating the attenuations

In this section, we discuss the construction of FUV attenuation estimates using the FUV/FIR ratio and outline the methods used to estimate the stellar $E(B-V)$ and the UV spectral slope β .

As discussed in §2, it is possible to estimate FUV attenuation using a FUV/FIR flux ratio. This can be done using a simple energy balance. However, we use the flux ratio method of Gordon et al. (2000) to estimate the attenuation, to allow us to fully take into account uncertainties due to dust geometry, type and

stellar populations. The 1500\AA attenuation derived using this method, as described in §2, is approximated to within 0.03 mag by eqn. 2.

To apply this method we construct an integrated FIR 8–1000 μm flux following Gordon et al. (2000). The 8.3 μm , 12 μm , 25 μm , 60 μm and 100 μm fluxes were numerically integrated to provide an estimate of the 8–120 μm flux. The 60 μm and 100 μm fluxes were then used to define a dust temperature for a $\beta = 1$ dust emissivity model to extrapolate to 1000 μm . This extrapolation, which adds typically $\sim 25\%$ to the flux, was tested against raw 178'' square aperture fluxes from the ISO archive. To within a constant scaling that accounts for aperture correction and pointing offsets, the fluxes and model extrapolations are within 10% of each other at 120 μm , 150 μm , and 200 μm . We assume no Lyman continuum ionizing radiation is absorbed by dust internal to the H II region: assuming that 50% of the ionizing radiation is absorbed by dust produces around a -0.15σ systematic offset in the estimated attenuation.

Alternatively, a more ‘standard’ manner to compute the attenuation of starlight from the central young cluster utilizes the measurement of reddening based on the optical stellar color excess $E(B-V)$. For 45 particular LMC H II regions, Caplan & Deharveng (1986) provide $E(B-V)$ values, which we correct for galactic foreground reddening. However, these values are average values for a number of stars *near* the H II region. Because some of these stars may be well in the foreground or background relative to the H II region, the average reddening does not necessarily reflect the attenuation toward the central star cluster in the H II region.

Finally, one can estimate the attenuation of the central star cluster using the UV spectral slope β , as estimated using the $1500\text{\AA} - 1900\text{\AA}$ color and as defined in eqn. 1. Uncertainties in β are derived from the random errors in the FUV flux, and typically become larger for more highly-reddened H II regions (as they are typically more attenuated and are therefore fainter). The β values of 4 UV-bright star formation regions were tested against $10'' \times 20''$ *International Ultraviolet Explorer* (IUE) UV spectral slopes. We find that 3/4 of the IUE β values agreed with the Rocket UV-derived β values to better than 0.5 in UV spectral slope. This is a remarkable agreement considering the huge differences in aperture size ($10'' \times 20''$ compared to a 4.9' diameter aperture). It is worth briefly noting that for these four H II regions with IUE spectra there is no evidence for a systematic difference between values of β derived using a synthetic $1500\text{\AA} - 1900\text{\AA}$ color and using the wavelength windows defined by Calzetti et al. (1994).

4.2.2. Comparing the attenuations

We show the direct comparison between UV spectral slope β and $A_{1500,\text{FR}}$ in Fig. 6. Despite the significant scatter, and considerable observational errors, there is a trend between β and 1500\AA attenuation. Two points are apparent immediately.

Firstly, the change in FUV spectral slope β for a given 1500\AA attenuation is *much* larger than expected using an average LMC extinction curve (solid line). Furthermore, the correlation is much steeper than the correlation between β and FUV attenuation derived for starbursting galaxies (open points) by Calzetti et al. (1994) and Meurer, Heckman, & Calzetti (1999). The steepness of the relationship between β and $A_{1500,\text{FR}}$ is likely due to radiative transfer effects, and does not imply that the dust in LMC H II regions is SMC-type: this point is discussed in detail in §5.2. The existence and steepness of the correlation

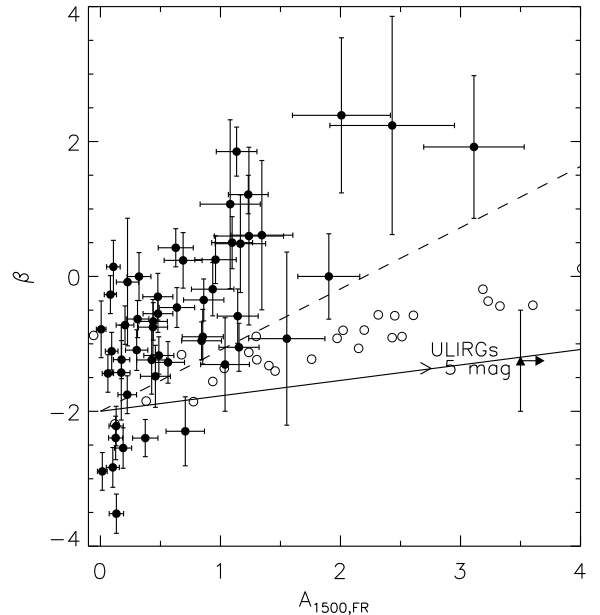


FIG. 6.— FUV spectral slope β against the 1500\AA flux ratio-derived attenuation $A_{1500,\text{FR}}$. Quantities were derived within the $4.9'$ aperture of Caplan & Deharveng (1985, 1986) for our sample of 52 H II regions. The solid line denotes the expected correlation assuming a typical LMC extinction curve and the dashed line the SMC extinction curve. These lines, also shown in Figs. 7–12, have been shown only to let the reader use their existing intuition to help understand the data; however, it is inappropriate to try differentiate between different extinction curves using these data because of the complicating effects of radiative transfer (see e.g. Figs. 2 and 12). An intrinsic β of -2.0 has been assumed. Open points denote the starburst sample of Calzetti et al. (1994): their values of β were calculated in a similar way to the LMC H II regions. Average results from Meurer et al. (2000) for a sample of 6 ultra-luminous infrared galaxies are also shown, which have estimated 1500\AA attenuations in excess of 5 magnitudes.

are robust: omitting the three points with highest $A_{1500,\text{FR}}$, or even one quarter of the data points with highest $A_{1500,\text{FR}}$, does not significantly change either the significance or slope of the correlation.

The open points were calculated using synthetic 1500\AA and 1900\AA fluxes derived from IUE spectra, and FIR luminosities calculated as above for the H II regions using data from Calzetti et al. (1994, 1995). Typical errors in β and $A_{1500,\text{FR}}$ for the starburst galaxies are ~ 0.1 and ~ 0.15 mag respectively, which is smaller than the (modest) scatter shown by the starbursts. Finally, we also show average results from Meurer et al. (2000) for a sample of 6 ultra-luminous infrared galaxies that have estimated 1500\AA attenuations in excess of 5 magnitudes.

This comparison of empirical results demonstrates directly that the correlation between β and FUV attenuation is highly variable. Although H II regions are arguably the basic unit of star formation, the behavior of the β -attenuation correlation differs strongly between H II regions and intensely star-forming galaxies.

Secondly, the scatter in the H II region β -attenuation correlation is large. This scatter indicates that the FUV spectral slope is not necessarily an accurate indicator of FUV attenuation, which is not surprising because the relationship between β and FUV attenuation is highly dependent on dust/star geometry and FUV extinction curve shape (e.g. Witt & Gordon 2000, see also Fig. 2). We discuss Fig. 6 in more detail in §5.2, while in-

vestigating possible reasons for the steep slope and scatter and discussing some implications of this result.

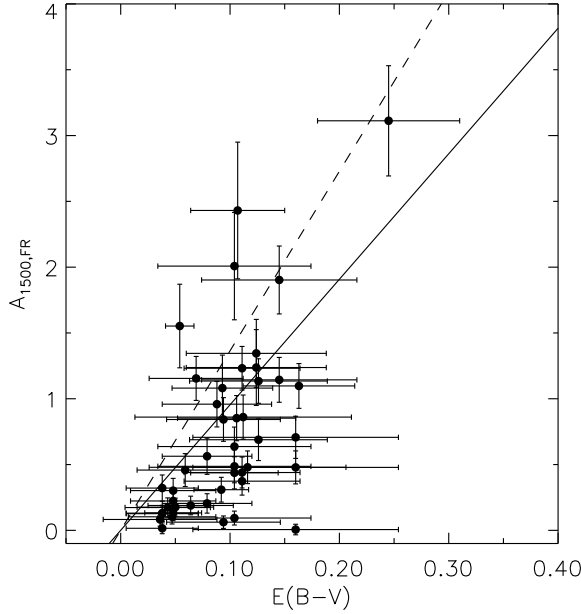


FIG. 7.— Optical color excess $E(B-V)$ against the 1500Å flux ratio-derived attenuation $A_{1500,FR}$. The $E(B-V)$ values were derived for the overall region around the 45 H II regions of interest. Flux ratio-derived attenuations were derived within a $4.9'$ aperture. The solid line denotes the expected correlation assuming a typical LMC extinction curve and the dashed line the SMC extinction curve.

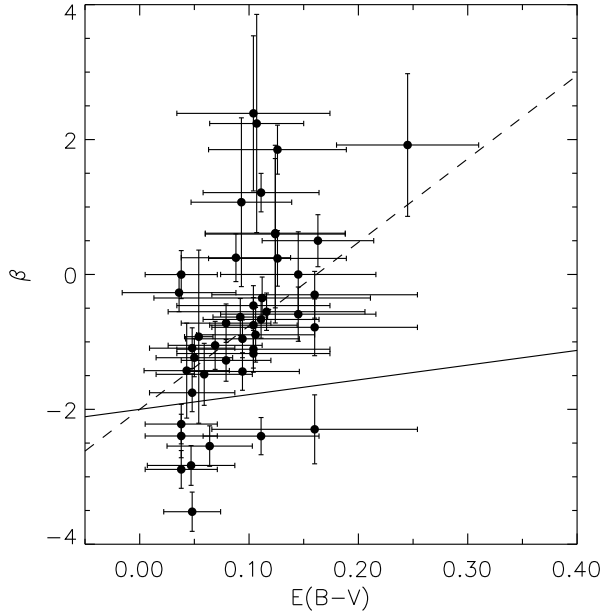


FIG. 8.— Optical color excess $E(B-V)$ against the UV spectral slope β derived within $4.9'$ apertures. Solid and dashed lines denote the expectations of a screen model with LMC-type and SMC Bar-type dust respectively.

FUV attenuation may be estimated from $E(B-V)$, in conjunction with assumptions regarding the extinction curve and

dust geometry. In Fig. 7, we show $A_{1500,FR}$ against $E(B-V)$. In Fig. 8, we show the UV spectral slope β against $E(B-V)$. Overplotted are expectations for the correlations assuming an average LMC extinction curve (solid line) and SMC bar extinction curve (dashed line). Despite the large scatters in both correlations, the correlations are significant at greater than the 99.9% level, with Spearman rank correlation coefficients of 0.57 ($A_{1500,FR}-E(B-V)$) and 0.54 ($\beta-E(B-V)$).

From this discussion, we conclude that the values of $A_{1500,FR}$, β and $E(B-V)$ for our sample of H II regions are broadly consistent: at the very least, as one increases, the other indicators tend to increase also. The large scatter in the correlation, however, demonstrates that the assumptions behind each of the methods are continually being violated to varying degrees.

4.3. Comparing H α and far-UV attenuation

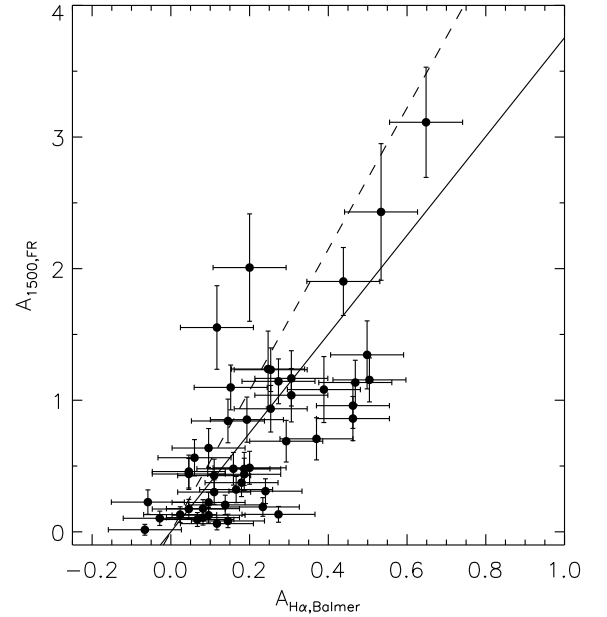


FIG. 9.— The 1500Å flux ratio-derived attenuation $A_{1500,FR}$ against the Balmer-derived H α attenuation $A_{H\alpha,Balmer}$. Attenuations were derived within the $4.9'$ aperture of Caplan & Deharveng (1985, 1986) for 50 of our 52 H II regions. Solid and dashed lines denote the expectations of a screen model with LMC-type and SMC Bar-type dust respectively.

We have tested H α and FUV attenuation estimates independently for internal consistency and now turn to cross-comparing them. Caplan & Deharveng (1986) found a highly scattered correlation between $E(B-V)$ to $A_{H\alpha,Balmer}$. We explore other correlations between H α and FUV attenuation indicators in Figs. 9 and 10, where we show the flux ratio-derived 1500Å attenuation, $A_{1500,FR}$, against the Balmer-derived H α attenuation, $A_{H\alpha,Balmer}$, and the radio-derived H α attenuation, $A_{H\alpha,Radio}$.

In Fig. 9 we plot $A_{1500,FR}$ against $A_{H\alpha,Balmer}$. Although there is considerable scatter, the overall correspondence between $A_{1500,FR}$ and $A_{H\alpha,Balmer}$ (significance > 99.9%; Spearman rank correlation coefficient of 0.72) is strong. The error-weighted mean ratio of $A_{1500,FR}/A_{H\alpha,Balmer}$ is 3.4 ± 0.3 with a RMS of 1.8 for 50 H II regions. This correspondence is as expected after accounting for radiative transfer effects (cf. panel (c) of Fig. 2).

In Fig. 10 we show the correlation between $A_{1500,FR}$ and $A_{H\alpha,Radio}$ (significance > 99.9%; Spearman rank correlation co-

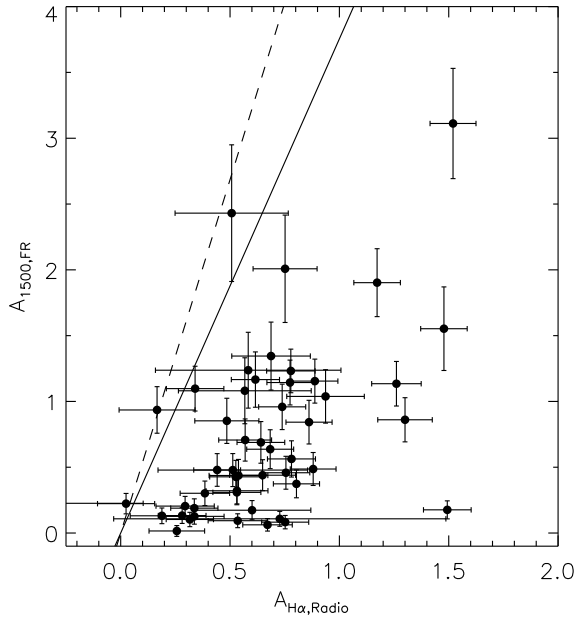


FIG. 10.— The 1500Å flux ratio-derived attenuation $A_{1500,FR}$ against the radio-derived $H\alpha$ attenuation $A_{H\alpha,Radio}$. Attenuations were derived within the 4.9' aperture of Caplan & Deharveng (1985, 1986) for 50 of our 52 H II regions. Solid and dashed lines denote the expectations of a screen model with LMC-type and SMC Bar-type dust respectively.

efficient of 0.47). The error-weighted mean ratio of $A_{1500,FR}/A_{H\alpha,Radio}$ is 1.3 ± 0.1 with a RMS of 0.7 for 50 H II regions. This relationship is more complex than the previous one between $A_{1500,FR}$ and $A_{H\alpha,Balmer}$. For example, there are a considerable number of H II regions with either much lower or higher $A_{H\alpha,Radio}$ than would be expected on the basis of the measured $A_{1500,FR}$. This extra scatter will be discussed in more detail below. Despite some oddities, there is a basic correspondence between $H\alpha$ and FUV attenuations in our sample of LMC H II regions, lending credibility to both sets of attenuation indicators.

5. DISCUSSION

The observed values of $A_{H\alpha,Balmer}$, $A_{H\alpha,Radio}$, $A_{1500,FR}$, β and $E(B-V)$ are generally consistent, especially given the uncertainties and the range of behaviors expected from radiative transfer effects. However, there are two discrepancies that deserve further discussion: the highly scattered correlation between $A_{H\alpha,Balmer}$ and $A_{H\alpha,Radio}$, and the deviant behavior of the highly scattered correlation between $A_{1500,FR}$ and β .

5.1. Are there problems with radio-based $H\alpha$ attenuations?

The systematic discrepancy between $A_{H\alpha,Radio}$ and $A_{H\alpha,Balmer}$ is well-known and generally attributed to a relatively gray effective attenuation curve, which is due to radiative transfer effects (e.g. Caplan & Deharveng 1986; van der Hulst et al. 1988; Ye 1998). We confirm the empirical result, but suggest that the interpretation should be examined in more detail. A comparison of Figs. 9 and 10 shows that the 1500Å attenuation correlates with considerable scatter with $A_{H\alpha,Balmer}$, but correlates with a much larger scatter with $A_{H\alpha,Radio}$. This behavior suggests a limitation in the values of $A_{H\alpha,Radio}$, rather than a limitation with $A_{H\alpha,Balmer}$. This runs contrary to the typical argument that $A_{H\alpha,Radio}$ is robust because it is oblivious to radiative transfer

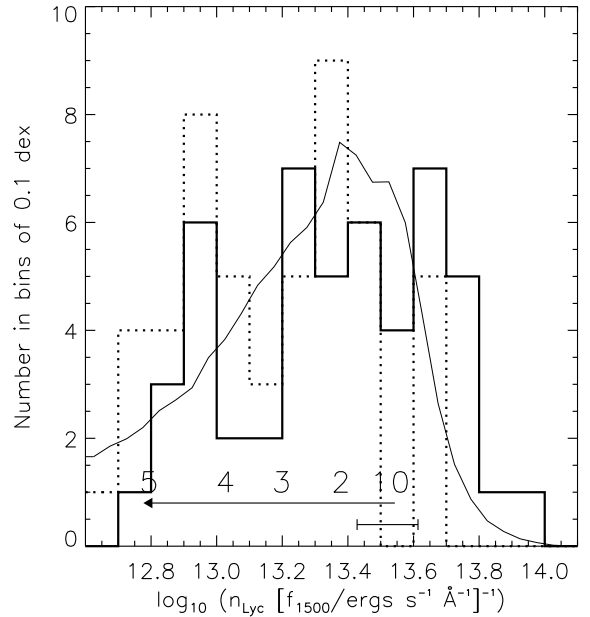


FIG. 11.— Distribution of the number of ionizing H II region photons, per unit 1500Å flux. The number of Lyman continuum photons required to produce the observed $H\alpha$ flux (assuming Case B recombination) has been corrected assuming radio-derived $H\alpha$ attenuations (thick solid line) and Balmer-derived $H\alpha$ attenuations (thick dotted line). The 1500Å flux has been corrected using the flux ratio method (the flux ratio method was earlier demonstrated to give attenuations which were not inconsistent with other attenuation indicators). The predicted ratio n_{Lyc}/f_{1500} is shown for a single burst PÉGASE model with a range of ages in Myr along the arrow at the bottom. This model assumes 1/3 solar metallicity: models with metallicities within a factor of three of this value give maximum ratios less than 0.05 dex different from the 1/3 solar model. We also show the effect of slope changes of ± 0.5 from the Salpeter value for the zero age point (error bar). Also shown is a model curve for $\sim 10^5$ simulated H II regions with ages between 0 and 6 Myr, and total stellar masses between $500M_{\odot}$ and $8000M_{\odot}$. Scatter from small number statistics at the upper end of the IMF and observational errors was accounted for (the curve for radio-derived errors is shown; the curve for Balmer-derived errors is essentially identical). Fluxes were derived within a 4.9' aperture.

effects.

We are in a position to explore the relationship between $A_{H\alpha,Balmer}$ and $A_{H\alpha,Radio}$ further than existing studies because of our expanded wavelength coverage. Previous studies often involved only the Balmer-derived and radio-derived attenuations (e.g. Caplan & Deharveng 1986; van der Hulst et al. 1988; Ye 1998), leaving the situation ambiguous. Other data (such as the UV and FIR fluxes) can be used, in principle, to shed new light on the problem.

One sensitive diagnostic is the $H\alpha$ -to-1500Å flux ratio. This ratio is a sensitive indicator of the temperature of the illuminating stellar population. Assuming Case B recombination, we convert this ratio into n_{Lyc}/f_{1500} , assuming 0.45 $H\alpha$ photons per Lyman continuum photon (Hummer & Storey 1987): we plot this in Fig. 11. Before converting the $H\alpha$ luminosities into the number of Lyman continuum photons, we correct for $H\alpha$ attenuation using either radio-derived (thick solid line) or Balmer-derived (thick dotted line) attenuations. The fraction of Lyman continuum photons absorbed by dust before being down-converted to $H\alpha$ and radio is not accounted for. The loss of Lyman continuum photons to dust prior to their conversion to Balmer photons would simply increase the estimated n_{Lyc}/f_{1500} : for reference, DeGioia-Eastwood (1992) estimates

the fraction of Lyman continuum photons lost to dust at between 0.2 and 0.5 for six LMC H II regions (corresponding to an underestimate of n_{Lyc}/f_{1500} of between 0.1 and 0.3 dex). The 1500Å flux is corrected for attenuation using the flux ratio-derived attenuations (as is apparent from Fig. 6, attenuations estimated from β and the calibration of Calzetti et al. (1994) would be implausibly large and are therefore not used here).

The radio-derived attenuations lead to larger n_{Lyc}/f_{1500} than the Balmer-derived attenuations. To be able to interpret the differences between the two sets of values, we show the expected range of n_{Lyc}/f_{1500} from the PÉGASE stellar population synthesis model (arrow; the numbers denote H II region age in Myr). The illustrated model has a metallicity of 1/3 solar. Changing the metallicity by a factor of three in either direction, or adopting the STARBURST99 model of Leitherer et al. (1999) results in systematic offsets of less than 0.05 dex. Changing the slope of the initial mass function from the Salpeter logarithmic slope, $x = -1.35$, by ± 0.5 results in changes of ∓ 0.1 dex in n_{Lyc}/f_{1500} at zero age (the error bar in Fig. 11). Comparison of the model predictions of n_{Lyc}/f_{1500} with the observations suggests that the radio-derived $A_{\text{H}\alpha, \text{Radio}}$ may be overcorrecting the H α luminosity, while the Balmer-derived $A_{\text{H}\alpha, \text{Balmer}}$ may be more appropriate.

To test the significance of this suggestion, we construct a simple model. The evolution of stellar populations in narrow mass ranges was calculated using the PÉGASE stellar population model. Around 10^5 randomly-generated stellar populations with ages between 0 and 6 Myr and total masses between $500M_{\odot}$ and $8000M_{\odot}$ were extracted from a Salpeter IMF. Model values of n_{Lyc}/f_{1500} were convolved with the observational errors. The model curve is shown in Fig. 11. There is a significant tail of model $\log_{10}(n_{\text{Lyc}}/f_{1500})$ values above the zero-age value of 13.55, which are attributable in part to the effects of observational error, and in part to small number statistics in populating the IMF of H II regions with massive stars. We find that the observed distribution corrected with radio-derived H α attenuations has a number of rather large values of n_{Lyc}/f_{1500} , but it is not inconsistent with model distributions. The distribution corrected with Balmer-derived H α attenuations is also consistent with model distributions.

So, while there is a definite discrepancy between observed values of $A_{\text{H}\alpha, \text{Balmer}}$ and $A_{\text{H}\alpha, \text{Radio}}$, it is not possible at this stage to identify unambiguously the limitations of each attenuation indicator. Folding in FUV and FIR data can, in principle, give further insight, and, indeed, there is a hint of limitations in the radio-derived H α attenuations. However, even given this extra data, it is impossible to rule out that the distribution of n_{Lyc}/f_{1500} , derived using radio-based H α attenuations, is consistent with plausible stellar populations. More detailed investigations, involving spatially-resolved maps of H II regions at H α , H β , and a number of radio frequencies, are required to fully address this question.

5.2. The relationship between β and $A_{1500, \text{FR}}$

In §4.2, we discussed the highly scattered and rather steep correlation between the UV spectral slope β and the 1500Å attenuation $A_{1500, \text{FR}}$. Both the slope and scatter of the correlation run counter to (at least) observational expectation: the correlation between β and $A_{1500, \text{FR}}$ for starbursting galaxies is tighter and shows a shallower slope. We discuss possible interpretations of the steepness and scatter in this correlation, and some implications of this result for studies of the UV properties of

high-redshift galaxies.

We first address the possibility that the steepness and scatter of this correlation reflect the data quality (or, for example, variations in Galactic foreground extinction), rather than the intrinsic properties of the H II regions. The quality of the data was discussed extensively in §§3.1 and 4.2. Briefly, the zeropoint uncertainties in the UV and FIR data used to construct the $A_{1500, \text{FR}}$ estimates are accurate to better than 10%. We have taken care to quantify and estimate appropriate sky level errors (§3.3), which are propagated into the final attenuation and UV spectral slope estimates. Furthermore, although the UV spectral slopes are difficult to check against external comparison data, we found an agreement of better than 0.5 in slope in 3/4 test cases (comparing values derived from $10'' \times 20''$ apertures with our values derived using a $4.9'$ aperture). We conclude that our error bars are fair, and that data quality issues are not likely to cause the large scatter and steep slope we see in Fig. 6 (re-plotted as Fig. 12). Variations in Galactic foreground extinction corresponding to $\Delta E(B-V)$ of ± 0.06 mag produce a negligible spectral slope change and variations in $A_{1500, \text{FR}}$ of ± 0.5 mag. This kind of variation is possible: Oestreicher, Goehrmann, & Schmidt-Kaler (1995) discussed the evidence for variable foreground extinction in the direction of the LMC, but with insufficient spatial resolution for our purposes. Given this, we conclude that variable foreground extinction can contribute significantly to the scatter, but cannot account for it in its entirety.

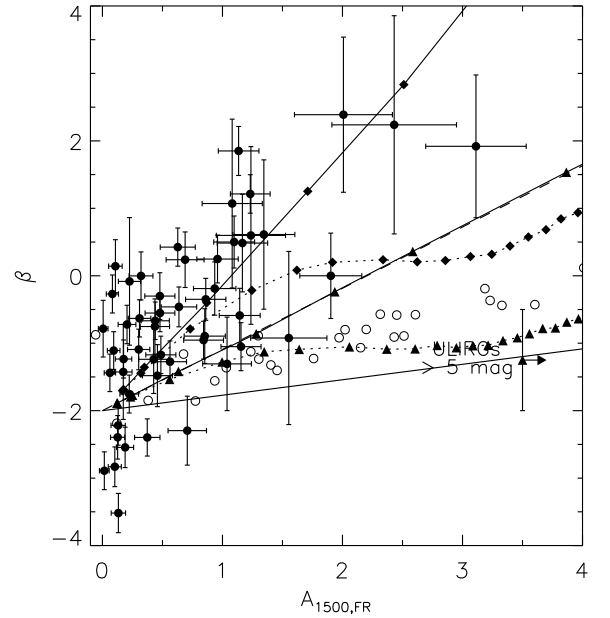


FIG. 12.— FUV spectral slope β against the 1500Å flux ratio-derived attenuation $A_{1500, \text{FR}}$. Symbols are as in Fig. 6. The solid line without symbols denotes the expected correlation assuming a typical LMC extinction curve. The dashed line (which is hidden under the solid line with triangles) denotes the SMC extinction curve. An intrinsic β of -2.0 has been assumed. These lines have been shown only to let the reader use their existing intuition to help understand the data; however, it is inappropriate to try differentiate between different extinction curves using these data because of the complicating effects of radiative transfer. To illustrate this point, radiative transfer model lines for LMC2-type dust (for a supershell near 30 Dor; triangles) and SMC bar-type dust (diamonds) with homogeneous (solid lines with symbols) and clumpy (dotted lines with symbols) geometries are overplotted.

We turn to intrinsic properties of the H II regions to explain the observation. No more than 0.05 dex of scatter in β and

0.15 mag of scatter in $A_{1500,FR}$ can be generated by appealing to small number statistics at the upper end of the H II region IMF: this scatter is much smaller than the observed scatter. A promising possibility is the combined influence of differing extinction curves and dust/star geometry: in §2 we demonstrated that these can strongly affect the relationship between $A_{1500,FR}$ and β . We demonstrate this more quantitatively in Fig. 12, where we replot Fig. 6, now including models from the DIRTY radiative transfer model. These models, in the spirit of the earlier inclusion of LMC and SMC screen models in earlier plots, are not meant to suggest that we are trying to differentiate between different geometries or extinction curves: rather, we are attempting to guide our intuition as to what effects can be plausibly caused by extinction curve and geometry variations.

Variations in H II region extinction curves and/or star/dust geometries can produce a steep slope *and* a large scatter in the β – $A_{1500,FR}$ plane. Slopes in this plot steeper than those produced by a simple screen are possible because of scattering (compare the SMC Bar-type extinction curve screen and shell model). However, deviations from a perfect shell introduce significant scatter and flatten the relation somewhat (the clumpy shell models have shallower slopes than the homogeneous shell models). Lastly, it may be possible to produce redder spectral slopes and very low $A_{1500,FR}$ values with either Galactic foreground extinction variations or small amounts of dust directly along the line of sight, which produce significant reddening but relatively little FIR luminosity.

We conclude that modest (and expected) variations in geometry can produce the steep slope of the β – $A_{1500,FR}$ correlation and at least some of the scatter. This result carries with it serious implications for the use of β as an accurate indicator of FUV attenuation. Neither ultra-luminous infrared galaxies nor our sample of LMC H II regions follow the relatively tight correlation between β and $A_{1500,FR}$ established for starbursting galaxies. However, this correlation is utilized extensively for the estimation of the SFRs of high-redshift galaxies (see e.g. Adelberger & Steidel 2000, for extensive testing of this correlation, and references therein). Although the high-redshift star-forming galaxies are likely to be more similar to the low-redshift starburst sample of Calzetti et al. (1994) than to our sample of LMC H II regions, it is nevertheless a concern that the basic units of star formation (H II regions) have a drastically different behavior from star-bursting galaxies. Clearly, much caution is warranted before estimating FUV attenuations based on UV spectral slopes.

6. SUMMARY

We have used FUV, $H\alpha$, FIR, and 8.55 GHz radio images of the LMC to investigate the SEDs and attenuations of H II regions drawn from the catalogs of Caplan & Deharveng (1985, 1986). We briefly discussed the relative morphologies of the LMC in the FUV, optical continuum, $H\alpha$, and FIR. In particular, the FUV and $H\alpha$ distributions within the LMC are different, implying that our findings regarding the effects of dust in the UV in LMC H II regions may not apply to the LMC as a whole.

We constructed SEDs for the sample of H II regions. The effects of attenuation on the SEDs are clear: H II regions with larger Balmer decrements show a larger FIR to UV luminosity ratio, and typically redder UV spectral slopes (Fig. 4). To quantify these trends, we constructed attenuation indicators of both the ionized H II region gas (the Balmer decrement and radio to $H\alpha$ luminosity ratio) and the stars (the UV spectral slope β , optical stellar reddening, and the balance of FUV and FIR

luminosity). Our principal findings are as follows.

- Estimates of $H\alpha$ and FUV attenuation all correlate, although often with substantial scatter (Figs. 5–10). Some of this scatter is due to errors in the (often quite modest) attenuations. However, much of this scatter is naturally interpreted in terms of radiative transfer in non-trivial dust/star geometries.
- The modest Balmer-derived $H\alpha$ attenuations are systematically lower than radio-derived $H\alpha$ attenuations. Previous studies have attributed this systematic offset to variations in the extinction within the beam. In principle, more insight can be gained by incorporating FUV and FIR fluxes. However, the inclusion of these data cannot, at this stage, unambiguously identify the source of the discrepancy between Balmer-derived and radio-derived $H\alpha$ attenuations. More work, involving spatially-resolved maps of $H\alpha$, $H\beta$, and radio emission at a range of frequencies, is required to properly investigate this issue.
- 1500Å attenuation and UV spectral slope β do correlate with each other (see Fig. 6), although with a large scatter and a substantially steeper slope than was expected on the basis of the LMC extinction curve or the empirically-derived correlation between A_{1500} and β for starbursting galaxies (Calzetti et al. 1994). Ultra-luminous infrared galaxies populate yet another part of A_{1500}/β space (Meurer et al. 2000). While some scatter may be due to variations in foreground galactic extinction, both the large scatter and variation in slope between a variety of star-forming systems demonstrates empirically that β is not necessarily an accurate indicator of FUV attenuation. This point has been argued extensively from a theoretical perspective (Fig. 2; Witt & Gordon 2000). This conclusion carries with it serious implications for the many studies of the rest frame UV properties of high-redshift galaxies that utilize the local correlation between β and $A_{1500,FR}$ for starbursting galaxies to (substantially) correct the observed UV fluxes for extinction. If, as is suggested by our work and the work of Meurer et al. (2000), the correlation between β and $A_{1500,FR}$ can have a variable slope and large scatter, serious thought must be devoted to the suitability of using β to correct UV fluxes for extinction.

We thank R. Cornett, J. Parker, M. Braun and M. Filipović for providing images of the LMC in the UV, R -band, FIR, and radio respectively. We also wish to thank the referee, Geoff Clayton, Daniella Calzetti and Claus Leitherer for their useful comments. E. F. B. and R. C. K. were supported by NASA grant NAG5-8426 and NSF grant AST-9900789. K. D. G. was supported by NASA grants NAGW-3168 and NAG5-7933. D. Z. was supported by NASA grant NAG5-3501 and NSF grant AST-9619576.

REFERENCES

- Adelberger, K. L., & Steidel, C. C. 2000, *ApJ*, 544, 218
 Bell, E. F., & Kennicutt Jr., R. C. 2001, *ApJ*, 548, 681
 Blain, A. W., Smail, I., Ivison, R. J., & Kneib, J.-P. 1999, *MNRAS*, 302, 632
 Bothun, G. D., & Thompson, I. B. 1986, *AJ*, 96, 877
 Braun, M., Assendorp, R., Bontekoe, D. J. M., Kester, T. R., & Richter, G. 1998, in *The Magellanic Clouds and Other Dwarf Galaxies*, Proceedings of the Bonn/Bochum-Graduieretenkolleg Workshop, held at the Physikzentrum Bad Honnef, Germany, January 19-22, 1998, eds. T. Richtler and J. M. Braun (Shaker Verlag: Aachen) 121
 Buat, V., Xu, C., 1996, *A&A*, 306, 61
 Calzetti, D., Kinney, A. L., Storchi-Bergmann, T. 1994, *ApJ*, 429, 582
 Calzetti, D., Bohlin, R. C., Kinney, A. L., Storchi-Bergmann, T., Heckman, T. M. 1995, *ApJ*, 443, 136
 Caplan, J., & Deharveng, L. 1985, *A&AS*, 62, 63
 Caplan, J., & Deharveng, L. 1986, *A&A*, 155, 297
 Charlot, S., & Fall, S. M. 2000, *ApJ*, 539, 718

- Clayton, G. C., Gordon, K. D., & Wolff, M. J. 2000, *ApJS*, 129, 147
- Condon, J. J., 1992, *ARA&A*, 30, 575
- Cram, L., Hopkins, A., Mobasher, B., Rowan-Robinson, M., 1998, *ApJ*, 507, 155
- DeGioia-Eastwood, K. 1992, *ApJ*, 397, 542
- Filipović, M. D., Haynes, R. F., White, G. L., & Jones, P. A. 1998, *A&AS*, 130, 421
- Fioc, M., & Rocca-Volmerange, B. 2001, in preparation
- Fitzpatrick, E. L. 1986, *AJ*, 92, 1068
- Fitzpatrick, E. L., Ribas, I., Guinan, E. F., de Warf, L. E., Maloney, F. P., Massa, D. 2001, *ApJ*, in press (astro-ph/0010526)
- Gordon, K. D., & Clayton, G. C. 1998, *ApJ*, 500, 816
- Gordon, K. D., Misselt, K. A., Witt, A. N., Clayton, G. C. 2001, *ApJ*, 551, 269
- Gordon, K. D., Clayton, G. C., Witt, A. N., Misselt, K. A. 2000, *ApJ*, 533, 236
- Heckman, T. M., Robert, C., Leitherer, C., Garnett, D. R., van der Rydt, F. 1998, *ApJ*, 503, 646
- Hummer, D. G., & Storey, P. J. 1987, *MNRAS*, 224, 801
- Israel, F. P., Kennicutt Jr., R. C. 1980, *Astrophys. Lett.*, 21, 1
- Kennicutt Jr., R. C. 1983, *ApJ*, 272, 54
- Kennicutt, R. C., Jr., Bresolin, F., Bomans, D. J., Bothun, G. D., & Thompson, I. B. 1995, *AJ*, 109, 594
- Leitherer, C., et al. 1999, *ApJS*, 123, 1
- Madau, P., Ferguson, H. C., Dickinson, M. E., Giavalisco, M., Steidel, C. C., Fruchter, A. 1996, *MNRAS*, 283, 1388
- Meurer, G. R., Heckman, T. M., & Calzetti, D. 1999, *ApJ*, 521, 64
- Meurer, G. R., Heckman, T. M., Seibert, M., Goldader, J., Calzetti, D., Sanders, D., & Steidel, C. C. 2000, to appear in 'Cold Gas and Dust at High Redshift', *Proc. JD9, IAU Manchester 2000*, ed. D. J. Wilner (astro-ph/0011201)
- Misselt, K. A., Clayton, G. C., Gordon, K. D. 1999, *ApJ*, 515, 128
- Misselt, K. A., Gordon, K. D., Clayton, G. C., & Wolff, M. J. 2001, *ApJ*, 551, 277
- Oestreich, M. O., Gochermann, J., & Schmidt-Kaler, T. 1995, *A&AS*, 112, 495
- Pagel, B. E. J., Edmunds, M. G., Fosbury, R. A. E., & Webster, B. L. 1978, *MNRAS*, 184, 569
- Price, S. D., Egan, M. P., Carey, S. J., Mizuno, D. R., & Kuchar, T. A. 2001, *AJ*, 121, 2819
- Puget, J. L., Léger, A. 1989, *ARA&A*, 27, 161
- Quillen, A. C., Yukita, M. 2001, *AJ*, 121, 2095
- Schlegel, D. J., Finkbeiner, D. P., & Davis, M., 1998, *ApJ*, 500, 525
- Smith, A. M., Cornett, R. H., & Hill, R. S. 1987, *ApJ*, 320, 609
- Steidel, C. C., Adelberger, K. L., Giavalisco, M., Dickinson, M., Pettini, M., 1999, *ApJ*, 519, 1
- Sullivan, M., Treyer, M. A., Ellis, R. S., Bridges, T. J., Milliard, B., Donas, J., 2000, *MNRAS*, 312, 442
- van der Hulst, J. M., Kennicutt Jr., R. C., Crane, P. C., Rots, A. H. 1988, *A&A*, 195, 38
- Witt, A. N., Gordon, K. D. 2000, *ApJ*, 528, 799
- Ye, T. 1998, *MNRAS*, 294, 422

TABLE 2
H II REGION FLUXES THROUGH 4.9' APERTURES

Name	1500Å (Jy)	1900Å (Jy)	H α (10^{-10} ergs s $^{-1}$ cm $^{-2}$)	8.3 μ m (Jy)	12 μ m (Jy)	25 μ m (Jy)	60 μ m (Jy)	100 μ m (Jy)	8.55 GHz (Jy)
N77E	0.077 \pm 0.012	0.145 \pm 0.016	1.32 \pm 0.07	2.71 \pm 0.28	3.07 \pm 0.24	10.5 \pm 0.3	91.5 \pm 3.5	128.0 \pm 10.8	0.261 \pm 0.015
N4AB	0.057 \pm 0.014	0.075 \pm 0.017	0.99 \pm 0.05	4.36 \pm 0.11	5.13 \pm 0.06	16.0 \pm 0.1	102.9 \pm 0.8	151.5 \pm 2.5	0.430 \pm 0.022
N79AB	0.186 \pm 0.012	0.499 \pm 0.033	1.86 \pm 0.11	6.99 \pm 0.28	7.03 \pm 0.37	28.6 \pm 0.5	191.9 \pm 7.5	288.0 \pm 20.4	0.663 \pm 0.038
N79DE	0.317 \pm 0.022	0.559 \pm 0.045	2.70 \pm 0.14	4.42 \pm 0.19	5.04 \pm 0.38	18.0 \pm 0.5	164.9 \pm 7.1	261.4 \pm 17.2	0.544 \pm 0.030
N81	0.067 \pm 0.015	0.146 \pm 0.033	0.61 \pm 0.12	2.86 \pm 0.16	3.37 \pm 0.25	6.9 \pm 0.4	61.2 \pm 7.2	98.6 \pm 12.6	0.115 \pm 0.022
N83	0.297 \pm 0.019	0.526 \pm 0.034	2.77 \pm 0.14	6.59 \pm 0.19	7.66 \pm 0.18	28.3 \pm 0.3	232.5 \pm 4.9	381.7 \pm 11.4	0.611 \pm 0.033
N11F	1.280 \pm 0.065	1.599 \pm 0.082	1.85 \pm 0.12	2.84 \pm 0.33	3.46 \pm 0.48	10.8 \pm 0.7	99.3 \pm 9.9	142.9 \pm 23.8	0.338 \pm 0.029
N11B	1.073 \pm 0.054	1.319 \pm 0.067	7.95 \pm 0.40	7.73 \pm 0.19	10.52 \pm 0.20	61.3 \pm 0.3	392.7 \pm 2.8	486.5 \pm 5.3	1.994 \pm 0.102
N91	0.706 \pm 0.035	0.997 \pm 0.050	2.86 \pm 0.14	3.66 \pm 0.09	4.47 \pm 0.09	19.4 \pm 0.2	164.1 \pm 2.5	219.0 \pm 6.7	0.521 \pm 0.031
N11CD	0.424 \pm 0.023	0.626 \pm 0.033	4.34 \pm 0.23	5.13 \pm 0.62	6.33 \pm 0.74	25.9 \pm 1.0	215.2 \pm 10.2	285.8 \pm 29.4	0.909 \pm 0.047
N11E	0.029 \pm 0.008	0.090 \pm 0.007	1.10 \pm 0.09	2.72 \pm 0.33	3.35 \pm 0.36	9.1 \pm 0.4	90.1 \pm 3.4	160.6 \pm 11.2	0.245 \pm 0.021
N23A	0.635 \pm 0.033	0.984 \pm 0.050	0.95 \pm 0.05	1.17 \pm 0.11	1.26 \pm 0.07	3.7 \pm 0.1	40.6 \pm 0.7	76.3 \pm 1.8	0.211 \pm 0.011
N103B	0.787 \pm 0.039	0.903 \pm 0.046	1.19 \pm 0.06	1.62 \pm 0.24	1.52 \pm 0.30	3.2 \pm 0.4	45.5 \pm 5.6	73.1 \pm 13.7	0.246 \pm 0.016
N105A	0.530 \pm 0.027	0.688 \pm 0.035	3.92 \pm 0.20	10.67 \pm 0.45	12.56 \pm 0.36	45.3 \pm 0.4	359.3 \pm 4.6	524.1 \pm 13.8	0.966 \pm 0.050
N113 S	0.764 \pm 0.041	0.914 \pm 0.053	2.75 \pm 0.14	9.10 \pm 0.36	10.60 \pm 0.31	41.7 \pm 0.4	304.5 \pm 7.4	458.9 \pm 20.3	0.629 \pm 0.037
N113 N	0.586 \pm 0.030	0.809 \pm 0.042	1.71 \pm 0.09	2.25 \pm 0.19	2.49 \pm 0.14	6.2 \pm 0.3	86.1 \pm 5.0	148.5 \pm 6.6	0.251 \pm 0.023
N30BC	0.181 \pm 0.009	0.335 \pm 0.017	1.40 \pm 0.07	3.17 \pm 0.08	3.07 \pm 0.05	8.7 \pm 0.1	82.8 \pm 0.9	130.1 \pm 3.0	0.132 \pm 0.015
N119	2.129 \pm 0.109	1.707 \pm 0.096	3.37 \pm 0.17	4.59 \pm 0.34	5.14 \pm 0.42	22.0 \pm 0.7	192.9 \pm 13.2	237.3 \pm 26.8	0.503 \pm 0.028
N120ABC	0.720 \pm 0.050	0.817 \pm 0.079	2.34 \pm 0.12	8.00 \pm 0.28	8.92 \pm 0.31	26.6 \pm 0.2	254.4 \pm 4.1	327.7 \pm 13.5	0.523 \pm 0.030
N44BC	1.408 \pm 0.070	1.262 \pm 0.063	4.15 \pm 0.21	8.85 \pm 0.19	11.16 \pm 0.24	54.0 \pm 0.2	375.7 \pm 2.9	516.3 \pm 8.9	0.970 \pm 0.051
N44I	0.490 \pm 0.025	0.686 \pm 0.035	1.70 \pm 0.09	3.86 \pm 0.28	4.75 \pm 0.28	15.7 \pm 0.4	172.0 \pm 4.9	227.0 \pm 12.0	0.346 \pm 0.039
N44D	0.140 \pm 0.007	0.319 \pm 0.016	1.90 \pm 0.10	4.96 \pm 0.25	6.03 \pm 0.31	19.9 \pm 0.3	188.4 \pm 6.1	261.0 \pm 15.9	0.433 \pm 0.026
N138A	0.098 \pm 0.007	0.156 \pm 0.011	0.83 \pm 0.04	2.97 \pm 0.21	3.15 \pm 0.17	6.5 \pm 0.3	68.0 \pm 6.3	130.5 \pm 14.6	0.108 \pm 0.015
N48AC	0.209 \pm 0.011	0.318 \pm 0.019	0.93 \pm 0.05	5.02 \pm 0.15	5.80 \pm 0.16	16.7 \pm 0.3	146.5 \pm 4.5	214.0 \pm 12.3	0.343 \pm 0.026
N51D	1.332 \pm 0.067	1.052 \pm 0.054	2.24 \pm 0.11	0.47 \pm 0.11	0.80 \pm 0.08	3.7 \pm 0.1	44.3 \pm 2.4	59.8 \pm 3.6	0.316 \pm 0.026
N51E	0.153 \pm 0.011	0.254 \pm 0.015	1.02 \pm 0.07	0.70 \pm 0.14	0.90 \pm 0.16	2.7 \pm 0.2	38.3 \pm 3.9	57.1 \pm 7.7	0.186 \pm 0.017
N143	0.256 \pm 0.027	0.295 \pm 0.043	0.72 \pm 0.06	0.43 \pm 0.17	0.77 \pm 0.29	2.6 \pm 0.5	30.7 \pm 4.2	58.2 \pm 9.8	0.140 \pm 0.031
N144AB	2.000 \pm 0.101	1.343 \pm 0.074	3.72 \pm 0.20	5.62 \pm 0.16	7.28 \pm 0.15	26.6 \pm 0.2	216.6 \pm 4.0	263.7 \pm 7.7	0.538 \pm 0.030
N51C	1.145 \pm 0.058	1.075 \pm 0.060	1.98 \pm 0.10	2.25 \pm 0.11	2.85 \pm 0.10	13.0 \pm 0.2	122.0 \pm 3.2	171.8 \pm 6.5	0.263 \pm 0.027
N51A	1.048 \pm 0.058	0.941 \pm 0.058	1.46 \pm 0.08	2.77 \pm 0.10	2.94 \pm 0.08	8.8 \pm 0.1	104.1 \pm 2.5	165.2 \pm 4.8	0.222 \pm 0.021
N148	0.250 \pm 0.018	0.342 \pm 0.026	0.94 \pm 0.08	2.54 \pm 0.21	2.79 \pm 0.20	5.1 \pm 0.2	76.4 \pm 3.8	133.5 \pm 8.9	0.172 \pm 0.012
N55 N	0.460 \pm 0.024	0.578 \pm 0.033	1.38 \pm 0.07	2.78 \pm 0.06	2.95 \pm 0.02	8.2 \pm 0.1	96.0 \pm 0.2	164.9 \pm 0.7	0.219 \pm 0.014
N55A	0.718 \pm 0.036	0.760 \pm 0.039	2.00 \pm 0.10	2.84 \pm 0.09	3.29 \pm 0.03	12.5 \pm 0.0	118.2 \pm 0.2	175.4 \pm 0.4	0.228 \pm 0.020
N57A	1.630 \pm 0.085	1.407 \pm 0.080	2.85 \pm 0.14	6.19 \pm 0.11	7.29 \pm 0.14	23.5 \pm 0.2	232.7 \pm 4.9	334.7 \pm 10.8	0.434 \pm 0.024
Fit A	0.252 \pm 0.039	0.410 \pm 0.078	0.68 \pm 0.07	0.95 \pm 0.16	1.24 \pm 0.13	2.5 \pm 0.2	40.5 \pm 2.7	71.8 \pm 5.3	0.052 \pm 0.024
N63A	0.455 \pm 0.023	0.551 \pm 0.028	1.02 \pm 0.06	1.57 \pm 0.13	1.54 \pm 0.07	6.4 \pm 0.1	58.8 \pm 1.2	91.2 \pm 3.4	0.452 \pm 0.024
N59A	0.283 \pm 0.017	0.359 \pm 0.025	5.44 \pm 0.27	7.66 \pm 0.14	9.34 \pm 0.14	45.9 \pm 0.2	327.7 \pm 2.8	443.1 \pm 5.7	1.376 \pm 0.071
N154A	0.344 \pm 0.023	0.454 \pm 0.037	2.99 \pm 0.24	6.35 \pm 0.42	7.27 \pm 0.41	23.3 \pm 0.3	257.9 \pm 14.6	365.9 \pm 29.8	0.521 \pm 0.045
N64AB	0.205 \pm 0.019	0.248 \pm 0.023	1.07 \pm 0.06	2.25 \pm 0.12	2.16 \pm 0.11	4.6 \pm 0.1	55.9 \pm 2.2	108.6 \pm 6.2	0.194 \pm 0.014
N158C	0.913 \pm 0.062	0.840 \pm 0.095	6.04 \pm 0.43	10.56 \pm 0.57	13.40 \pm 0.77	72.0 \pm 1.6	538.8 \pm 33.6	665.2 \pm 54.8	1.138 \pm 0.064
N160AD	0.262 \pm 0.027	0.435 \pm 0.055	7.36 \pm 0.39	21.07 \pm 0.72	26.03 \pm 0.94	120.3 \pm 2.3	815.5 \pm 34.7	970.3 \pm 62.8	2.418 \pm 0.123
N158	0.341 \pm 0.019	0.524 \pm 0.036	2.43 \pm 0.47	2.44 \pm 0.65	3.18 \pm 0.72	15.3 \pm 3.5	140.2 \pm 45.1	151.2 \pm 61.8	0.435 \pm 0.104
N159	0.099 \pm 0.023	0.271 \pm 0.041	6.21 \pm 0.32	21.44 \pm 0.72	30.73 \pm 0.95	170.0 \pm 1.7	1153.3 \pm 24.8	1253.1 \pm 53.1	2.808 \pm 0.142
N158A	0.363 \pm 0.026	0.493 \pm 0.040	1.33 \pm 0.65	0.16 \pm 0.83	0.61 \pm 1.11	1.8 \pm 4.0	10.6 \pm 46.7	1.7 \pm 72.5	0.218 \pm 0.137
N160BCE	0.307 \pm 0.021	0.439 \pm 0.034	4.51 \pm 0.24	6.79 \pm 0.64	8.14 \pm 0.87	36.9 \pm 1.8	369.6 \pm 26.9	526.6 \pm 60.4	1.026 \pm 0.051
N175	0.020 \pm 0.003	0.023 \pm 0.003	0.47 \pm 0.03	0.26 \pm 0.75	0.52 \pm 0.98	1.1 \pm 0.9	19.2 \pm 15.6	32.8 \pm 46.1	0.123 \pm 0.017
N214C	0.077 \pm 0.005	0.145 \pm 0.011	2.28 \pm 0.11	1.13 \pm 0.17	1.98 \pm 0.12	8.2 \pm 0.1	80.2 \pm 0.9	130.4 \pm 3.7	0.348 \pm 0.031
NGC 2100	0.338 \pm 0.024	0.583 \pm 0.042	0.43 \pm 0.23	1.31 \pm 0.46	1.46 \pm 0.47	2.0 \pm 1.5	25.7 \pm 23.2	46.0 \pm 46.7	0.093 \pm 0.042
N164	0.093 \pm 0.019	0.182 \pm 0.037	2.34 \pm 0.21	2.62 \pm 0.58	3.25 \pm 0.54	14.3 \pm 1.1	163.4 \pm 15.3	210.7 \pm 35.7	0.492 \pm 0.061
N165	0.043 \pm 0.011	0.083 \pm 0.017	0.54 \pm 0.08	1.05 \pm 0.26	1.12 \pm 0.22	2.8 \pm 0.4	64.8 \pm 3.1	95.5 \pm 10.5	0.103 \pm 0.037
N163	0.019 \pm 0.007	0.056 \pm 0.010	1.27 \pm 0.14	3.16 \pm 0.29	3.82 \pm 0.30	8.6 \pm 0.6	93.5 \pm 10.4	160.9 \pm 23.7	0.227 \pm 0.046
N180AB	0.357 \pm 0.018	0.515 \pm 0.026	3.44 \pm 0.17	2.90 \pm 0.11	3.19 \pm 0.22	13.3 \pm 0.2	120.6 \pm 2.6	199.2 \pm 11.3	0.577 \pm 0.032

TABLE 3
H II REGION ATTENUATION ESTIMATES AND UV SPECTRAL SLOPES THROUGH 4.9' APERTURES

Name	$A_{H\alpha, \text{Balmer}}$ (mag)	$A_{H\alpha, \text{Radio}}$ (mag)	$A_{1500, \text{FR}}$ (mag)	$A_{1900, \text{FR}}$ (mag)	β
N77E	0.31 \pm 0.09	0.62 \pm 0.11	1.17 \pm 0.21	0.72 \pm 0.20	0.48 \pm 0.72
N4AB	0.12 \pm 0.09	1.48 \pm 0.11	1.55 \pm 0.32	1.28 \pm 0.30	-0.92 \pm 1.28
N79AB	0.47 \pm 0.09	1.26 \pm 0.11	1.13 \pm 0.17	0.52 \pm 0.16	1.85 \pm 0.36
N79DE	0.29 \pm 0.09	0.64 \pm 0.11	0.69 \pm 0.16	0.39 \pm 0.13	0.24 \pm 0.41
N81	0.39 \pm 0.09	0.57 \pm 0.30	1.08 \pm 0.25	0.57 \pm 0.22	1.07 \pm 1.25
N83	0.46 \pm 0.09	0.74 \pm 0.11	0.96 \pm 0.17	0.58 \pm 0.17	0.25 \pm 0.35
N11F	0.07 \pm 0.09	0.54 \pm 0.14	0.09 \pm 0.05	0.07 \pm 0.05	-1.11 \pm 0.28
N11B	0.20 \pm 0.09	0.88 \pm 0.10	0.49 \pm 0.13	0.37 \pm 0.12	-1.17 \pm 0.28
N91	0.24 \pm 0.09	0.53 \pm 0.11	0.31 \pm 0.09	0.21 \pm 0.09	-0.63 \pm 0.28
N11CD	0.10 \pm 0.09	0.68 \pm 0.11	0.64 \pm 0.15	0.42 \pm 0.13	-0.46 \pm 0.30
N11E	0.20 \pm 0.09	0.75 \pm 0.15	2.01 \pm 0.41	1.06 \pm 0.20	2.39 \pm 1.15
N23A	0.15 \pm 0.09	0.75 \pm 0.11	0.08 \pm 0.05	0.05 \pm 0.05	-0.27 \pm 0.28
N103B	0.12 \pm 0.09	0.67 \pm 0.11	0.06 \pm 0.05	0.06 \pm 0.05	-1.44 \pm 0.28
N105A	0.15 \pm 0.09	0.86 \pm 0.11	0.84 \pm 0.17	0.64 \pm 0.17	-0.95 \pm 0.28
N113 S	0.06 \pm 0.09	0.78 \pm 0.11	0.56 \pm 0.14	0.45 \pm 0.14	-1.27 \pm 0.31
N113 N	0.14 \pm 0.09	0.29 \pm 0.13	0.20 \pm 0.07	0.14 \pm 0.07	-0.72 \pm 0.28
N30BC	...	-0.18 \pm 0.15	0.63 \pm 0.15	0.34 \pm 0.12	0.42 \pm 0.28
N119	-0.03 \pm 0.09	0.32 \pm 0.11	0.10 \pm 0.05	0.13 \pm 0.07	-2.83 \pm 0.29
N120ABC	0.05 \pm 0.09	0.76 \pm 0.11	0.46 \pm 0.12	0.38 \pm 0.13	-1.48 \pm 0.46
N44BC	0.18 \pm 0.09	0.80 \pm 0.11	0.37 \pm 0.11	0.39 \pm 0.13	-2.40 \pm 0.28
N44I	0.05 \pm 0.09	0.65 \pm 0.15	0.44 \pm 0.12	0.30 \pm 0.11	-0.67 \pm 0.28
N44D	0.25 \pm 0.09	0.78 \pm 0.11	1.23 \pm 0.17	0.67 \pm 0.18	1.21 \pm 0.29
N138A	0.25 \pm 0.09	0.17 \pm 0.17	0.94 \pm 0.18	0.62 \pm 0.17	-0.19 \pm 0.40
N48AC	0.46 \pm 0.09	1.30 \pm 0.12	0.86 \pm 0.17	0.58 \pm 0.16	-0.35 \pm 0.31
N51D	-0.07 \pm 0.09	0.26 \pm 0.13	0.02 \pm 0.04	0.04 \pm 0.04	-2.89 \pm 0.28
N51E	0.17 \pm 0.09	0.53 \pm 0.14	0.32 \pm 0.10	0.18 \pm 0.08	-0.00 \pm 0.36
N143	0.05 \pm 0.09	0.60 \pm 0.27	0.17 \pm 0.07	0.14 \pm 0.08	-1.43 \pm 0.70
N144AB	0.27 \pm 0.09	0.28 \pm 0.11	0.13 \pm 0.06	0.20 \pm 0.08	-3.52 \pm 0.29
N51C	0.02 \pm 0.09	0.19 \pm 0.14	0.13 \pm 0.06	0.14 \pm 0.07	-2.22 \pm 0.29
N51A	0.10 \pm 0.09	0.34 \pm 0.14	0.13 \pm 0.06	0.14 \pm 0.07	-2.40 \pm 0.32
N148	0.19 \pm 0.09	0.54 \pm 0.13	0.44 \pm 0.12	0.30 \pm 0.11	-0.75 \pm 0.41
N55 N	0.11 \pm 0.09	0.38 \pm 0.11	0.30 \pm 0.09	0.23 \pm 0.09	-1.09 \pm 0.30
N55A	0.10 \pm 0.09	0.02 \pm 0.13	0.22 \pm 0.08	0.20 \pm 0.08	-1.75 \pm 0.28
N57A	0.23 \pm 0.09	0.34 \pm 0.11	0.19 \pm 0.07	0.21 \pm 0.09	-2.54 \pm 0.30
Fil A	-0.06 \pm 0.09	-0.41 \pm 0.51	0.23 \pm 0.09	0.13 \pm 0.08	-0.08 \pm 0.95
N63A	0.08 \pm 0.09	1.49 \pm 0.11	0.18 \pm 0.07	0.14 \pm 0.07	-1.23 \pm 0.28
N59A	0.50 \pm 0.09	0.89 \pm 0.11	1.15 \pm 0.17	0.94 \pm 0.20	-1.05 \pm 0.36
N154A	0.19 \pm 0.09	0.49 \pm 0.15	0.85 \pm 0.17	0.64 \pm 0.18	-0.89 \pm 0.41
N64AB	0.11 \pm 0.09	0.53 \pm 0.12	0.43 \pm 0.13	0.33 \pm 0.12	-1.24 \pm 0.51
N158C	0.37 \pm 0.09	0.57 \pm 0.12	0.71 \pm 0.16	0.70 \pm 0.20	-2.30 \pm 0.51
N160AD	0.44 \pm 0.09	1.17 \pm 0.11	1.90 \pm 0.26	1.41 \pm 0.24	-0.00 \pm 0.63
N158	0.19 \pm 0.09	0.51 \pm 0.34	0.48 \pm 0.13	0.30 \pm 0.11	-0.30 \pm 0.35
N159	0.65 \pm 0.09	1.52 \pm 0.11	3.11 \pm 0.42	2.10 \pm 0.30	1.92 \pm 1.06
N158A	0.16 \pm 0.09	0.42 \pm 0.87	0.01 \pm 0.04	0.01 \pm 0.04	-0.78 \pm 0.42
N160BCE	0.27 \pm 0.09	0.77 \pm 0.11	1.14 \pm 0.17	0.86 \pm 0.20	-0.59 \pm 0.40
N175	0.31 \pm 0.09	0.94 \pm 0.18	1.04 \pm 0.20	0.87 \pm 0.22	-1.31 \pm 0.69
N214C	0.15 \pm 0.09	0.34 \pm 0.13	1.10 \pm 0.17	0.66 \pm 0.18	0.50 \pm 0.39
NGC 2100	0.08 \pm 0.09	0.73 \pm 0.76	0.11 \pm 0.06	0.06 \pm 0.05	0.14 \pm 0.39
N164	0.50 \pm 0.09	0.69 \pm 0.18	1.34 \pm 0.26	0.86 \pm 0.25	0.61 \pm 1.11
N165	0.25 \pm 0.09	0.58 \pm 0.42	1.24 \pm 0.29	0.77 \pm 0.24	0.60 \pm 1.32
N163	0.53 \pm 0.09	0.51 \pm 0.26	2.43 \pm 0.52	1.40 \pm 0.28	2.24 \pm 1.62
N180AB	0.16 \pm 0.09	0.44 \pm 0.11	0.48 \pm 0.12	0.32 \pm 0.11	-0.55 \pm 0.28

This figure "f3.gif" is available in "gif" format from:

<http://arXiv.org/ps/astro-ph/0108367v2>